REGISTRATION OF MULTIMODAL DENTAL AND FACIAL IMAGES

ZHAO BAOPING

(B.Eng., Zhejiang University)

A THESIS SUBMITTED

FOR THE DEGREE OF MASTER OF ENGINEERING

DEPARTMENT OF ELECTRICAL AND COMPUTER ENGINEERING

NATIONAL UNIVERSITY OF SINGAPORE

2004

Acknowledgments

Many people have helped me to accomplish my research work and this thesis. They include my supervisors, my friends and my families. Without them, this achievement could only be a dream for me.

First, I would like to express my sincere thanks and gratitude to my supervisors, Assoc. Prof. Ong Sim Heng and Assoc. Prof. Kelvin Foong, for their imparting invaluable knowledge and providing excellent guidance during the entire progress of this research.

In addition, I would like to thank the officer in the Vision & Image Processing Laboratory, Mr. Francis Hoon for being so friendly, supportive and helpful during the course of this project.

I would also like to extend my appreciation to the following colleagues working in the Vision and Image Processing Lab, who have rendered their assistance and provided ideas for this project in one way or another: Ms. Ge Yi, Ms. Yang Mei, Dr. Xiao Gaoyu, Mr. Zhang Hua, Mr. Yan Pinkun, Mr. Shen Weijia and many others.

Finally, to my beloved parents, for the endless love and encouragement that I have grown up with for so many years since my childhood. I know you are there for me, always.

Contents

List of Figures

List of Tables

Summary

Different medical imaging modalities produce complementary diagnostic information. The integration and registration of the different image types will provide information that is useful to the clinician for diagnosis and treatment planning. Image data that are of interest to the dentofacial clinicians (e.g., orthodontists and oral surgeon) include cephalograms, dental casts, and facial shape models. This thesis presents a dentofacial registration system for registering the 3D images of the dental cast and facial shape model of the same patient.

Both 3D images contain only the surface data and there is no direct common information between them; thus the lateral cephalogram is used as a bridge relating them with each other. The entire project is subdivided into two parts: one is the registration of the facial model and the lateral cephalogram, and the other is that of the dental cast and the lateral cephalogram. For the former, a facial profile-based method is proposed to map the 2D lateral cephalogram onto the 3D facial model, while for the latter, a landmark-based approach is applied. Finally, the dental cast data and facial shape model are integrated and visualized.

Four different types of experiments were conducted to investigate the performance of the important intermediate steps involved in the entire dentofacial registration system. In the first experiment, the system's ability to extract facial profile from the lateral cephalogram and 3D facial model was tested. It was found that the system gave 87.5% accuracy in facial profile extraction. In the second experiment, the proposed facial-profile-based registration method, which determined the system's ability to

superimpose a lateral cephalogram onto the corresponding 3D facial model, was examined by registering a facial profile and itself with different pose and size. It was found that the angle error in the rotation transformation was much less than 1°, the scaling error was close to zero, and the translation error is within 1 to 2 pixels. The third experiment aimed to test the alignment of maxillary and mandibular dental casts, which were involved in the registration of dental casts with the cephalogram. In the last experiment, a new set of data was input to the registration system. The resultant integrated image was studied and the system accuracy was measured by the angle between the Po-Or plane and the occlusal plane. The error of this angle was 0.3539°, which is quite small and within the standard tolerance (1°).

Chapter 1 Introduction

1.1 Background

Orthodontics and dentofacial orthopedics is that area of dentistry concerned with the supervision, guidance and correction of the growing or mature dentofacial structures, including those conditions that require movement of teeth or correction of malrelationships and malformations of their related structures and the adjustment of relationships between and among teeth and facial bones by the application of forces or the stimulation and redirection of functional forces within the craniofacial complex, or both (definition/designation adopted by the ADA October, 1994) [1].

Before the introduction of radiographic cephalometry, dentalfacial orthopedic treatment planning was based primarily on observations of facial form and dental relationships. With the improvements in cephalometric analysis and evaluation, orthodontists became more aware of underlying jaw disproportion in the etiology of malocclusion. Also, analyses and treatment methods designed to address both the dental and facial skeletal components of orthodontic problems became more universal. Generally, orthodontists base their diagnosis on the craniofacial information provided by lateral cephalograms (Figure 1.1) and plaster dental casts (Figure 1.2).

Figure 1.1: A typical lateral cephalogram image

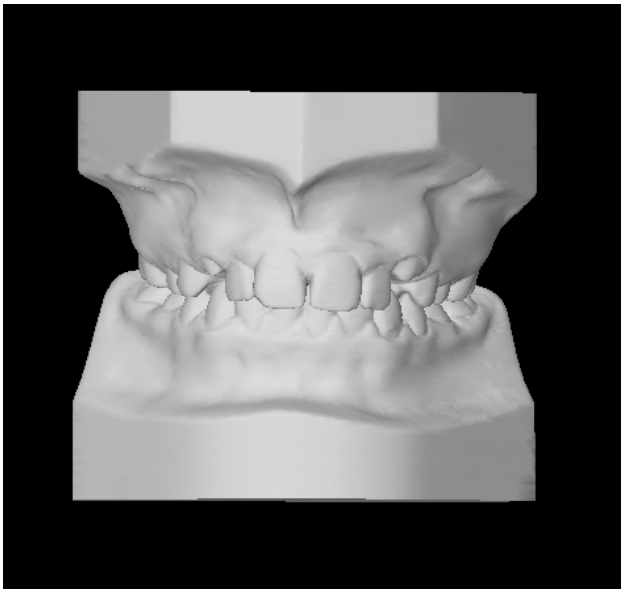

Figure 1.2: A set of plaster dental casts

Advances in computer technology have resulted in an increasingly significant role of computer vision in the practice of orthodontics. To provide orthodontists with a multifaceted view of the dental imagery, multimodality registration is necessary for the images often used for clinical analysis. More and more systems involving multimodality registration have been developed to assist in automatic orthodontic diagnosis and treatment planning. An example is the use of computerized imaging technology in virtual craniofacial patient project carried out by the Craniofacial Virtual Reality Laboratory and the Integrated Media Systems Center at the University of Southern California [2]. Their work was targeted at building a virtual craniofacial patient from CT data, digital teeth models, and human jaw motion tracking, which would enable researchers to develop methods for surgery simulation and treatment planning, among others.

Baumrind *et al.* [3] worked on the capture and rigorous analysis of information on craniofacial growth and the effects of therapeutic interventions. They developed a system merging 3D study casts and 2D lateral and frontal cephalograms, as well as 2D facial photographs.

Sarver [4] developed a videocephalometric system, in which the patient's profile image was gathered, integrated and calibrated with the cephalogram. Treatment options are then tested on the videocephalogram and the patient's profile adjusted accordingly by a computer program to reflect changes in the patient's appearance. This allows the patient and clinician to visualize the facial effect of orthodontic treatments.

Hajeer *et al*. [5] reviewed many 3D techniques that have been utilized to register and analyze the face in three dimensions, and also discussed each system's merits and

disadvantages. They developed a relatively new 3D imaging system called C3D to capture the 3D geometry of the face. Landmark identification on 3D facial models is facilitated by a software-based facial analysis tool. This system is very useful in studying facial soft tissue changes following orthognathic surgery and other types of facial surgery, as well as assessing facial soft tissue growth and development of the craniofacial complex.

Noguchi and Goto [6] have developed a simulation model of an orthognathic patient from the integration of the morphological data of the teeth and face, frontal and lateral cephalograms, and jaw templates by using commercial software (*Surfacer*, Imageware Inc., Ann Arbor, MI, USA). Their objective is similar to ours in that it aims to simulate a 3D model without using CT data. The differences are that the frontal cephalogram and jaw template are not involved in our project, and we developed a set of algorithms to integrate all the data, unlike [3], which directly processed the data manually using *Surfacer*. This commercial software provides tools for the direct creation of free-form surfaces from curves, surfaces, or measured data. It allows the user to input a 3D object in the form of digitized data and contains routines for manipulating, analyzing and visualizing the object.

The systems mentioned above have shown their utilities in certain clinical areas. However, although their targets are quite similar to ours, the solutions are different. For example, some of the systems [2,3] require metallic or ceramic markers to be placed on the objects being imaged, and these extrinsic features will facilitate the registration, while our approach is based on the intrinsic features of 3D models. More importantly, the current systems have some limitations.

(1) The key issue during the development of these systems is multimodal registration, which relies on common features present in the various datasets. However, this key step is simplified in [6] by using a commercial software, *Surfacer*, that requires extensive user input.

(2) The 3D facial models required in some systems [2] are obtained via CT scanning, which is radiologically invasive.

(3) Information extracted from facial soft tissue is provided by standard 2D photographs [3], which are not fully representative of the actual 3D face.

(4) Some systems [3,5] only focus on the registration of 3D dental casts with lateral or frontal cephalograms, or merely study the 3D facial models. This may limit their application in dentofacial orthodontics.

This thesis presents a new dentofacial registration system seeking to overcome the limitations mentioned above.

1.2 Project Overview

1.2.1 Rationale

Prior to making the definitive diagnosis of orthodontic problems, records of the patient's teeth, craniofacial skeleton and facial shape are routinely taken. These records are the dental casts, the lateral cephalogram, and photographs of the teeth and face. Information from these records is then mentally assembled by the orthodontist

to form the basis for a diagnostic assessment. To obtain 3D volume information of the teeth and skeletal structures, patients would have to undergo ionizing radiation from multi-slice helical CT scanning. Even with the advent of cone-beam CT for the craniofacial region, radiation exposure is substantially higher than that received from a lateral cephalogram. The direction in this research is therefore to create a 3D environment of the craniofacial region with the least exposure of ionizing radiation to the patients.

1.2.2 Description of the Registration System

The aim of this project is to develop a system that registers dental data in the form of dental casts, cephalograms, and facial models, and allows orthodontists to accurately visualize all the 3D data in the created virtual facial environment. Routine clinical records of the orthodontic patients will be converted into a digital platform as follows: (1) the dental casts will be digitized with a surface laser scanner (Figure 1.2); (2) the lateral cephalogram will be scanned (Figure 1.1), and (3) the facial shape will be acquired and digitized with a 3D surface light scanner (Figure 1.3). The 2D digital image of the lateral cephalogram will be merged in accurate spatial relationship with the 3D images of the dental casts and facial shape model. The resultant registration system permits the creation of a virtual 3D dental and facial environment for orthodontic diagnosis and treatment planning to be performed with the least amount of ionizing radiation to the patients. Through the accurate merging of the three different image modalities in this registration system, subsequent enhancements to it will take the form of merging accurate 3D root shapes to the 3D crowns of the teeth

on the dental casts. Simulation of tooth movements within the created 3D virtual dental and facial environment will permit the clinician to visualize how the changes in the spatial position of the teeth affect the spatial position of the lips and facial contours.

Figure 1.3: A facial model scanned by Geometrix Facevison scanner

1.3 Thesis Organization

General techniques for multimodal medical registration are reviewed with a specific emphasis on 3D/2D registration techniques in Chapter 2. Also, an overview of geometrical transformations is presented.

Chapter 3 presents the algorithm for 3D facial shape model registration with the lateral cephalogram. The chapter initially reviews the methods of facial profile analysis. Techniques for extracting facial profile and soft tissue landmarks (fiducial

points) on 2D X-rays and 3D facial models are presented. Subsequently, a registration method is proposed to register facial profiles. Finally, the chapter presents the implementation and registration results

Chapter 4 initially describes the method for the alignment of maxillary and mandibular dental casts, then presents the algorithm for the registration between cephalograms and 3D dental casts. Finally, the geometric transformation between the dental casts and the facial shape model is derived based on the registration results obtained in Chapter 3 and Chapter 4.

Chapter 5 provides the experimental results and discussion. Four different types of experiments are designed to test the performance of the intermediate steps involved in the entire project, namely, facial profile extraction, facial profile-based registration, alignment of upper and lower dental casts, and integration of facial and dental images.

Finally, we conclude in Chapter 6 with a summary of the results, the implications of these results on the proposed dentofacial registration system and suggestions for future work.

Chapter 2 Medical Image Registration

Medical imaging techniques provides the clinician with an increasingly multifaceted view of organ function and anatomy. The information provided by various imaging modalities is often complementary (i.e., provides separate but useful information) and synergistic (i.e., the combination of the information provides useful extra information). For example, X-ray computed tomography (CT) and magnetic resonance imaging (MRI) exquisitely demonstrate anatomy but provide little information about tissue functionalities. Furthermore, CT and MR images describe complementary morphologic features. Positron emission tomography (PET) and single photon emission computed tomography (SPECT) scans display aspects of function and allow metabolic measurements but poorly delineate anatomy. Hence, clinical diagnosis and therapy planning and evaluation are increasingly relying on complementary image information.

Images coming from different sources must be viewed and analyzed together. These multiple images, arranged in an organized manner so that the viewed objects are properly positioned in all of the particular images to form a coherent composition, are called multimodal images. The process of overlaying one image over the other, to obtain a multimodal image, is defined as the term image registration. Here, the image generically includes a 3D image (CT, MRI, SPECT or PET), a 2D image (x-ray projections captured on film or as a digital radiograph), or the physical arrangement of an object in space taken at different times, from different sensors or from different viewpoints.

2.1 Overview of Registration Methods

Over the years, a broad range of registration methods have been developed for the various types of data and applications. Therefore a number of classifications of these image registration methods have been proposed. They can be found in the papers by Brown [7], Mauer and Fitzpatrick [8], Maintz and Viergever [9] and Van der Elsen *et al*. [10]. Generally, the criteria of classification can be outlined as follows: (1) image dimensionality; (2) registration basis; (3) geometrical transformation; (4) degree of interaction; (5) optimization procedure; (6) modalities; (7) subject; and (8) object [11].

"Image dimensionality" refers to the number of geometrical dimensions of the image spaces involved, which are typically 3D but sometimes 2D in medical applications. The "registration basis" is the aspect of the two views used to effect the registration. For example, the registration might be based on a given set of point pairs that are known to correspond or the basis might be a set of corresponding surface pairs.

"Geometrical transformation" refers to the mathematical form of the geometrical mapping used to align points in one space with those in the other. "Degree of interaction" refers to the control exerted by a human operator over the registration algorithm. The ideal situation is fully automatic algorithm, which requires no interaction. "Optimization procedure" refers to the standard approach in algorithmic registration in which the quality of the registration is estimated continually during the registration procedure in terms of some function of the images and the mapping between them.

"Modalities" refers to the means by which the images to be registered are acquired. Examples are listed at the beginning of this chapter. "Subject" refers to patient involvement and comprises three subcategories: intrapatient, interpatient, and atlas. The latter category comprises registrations between patients and atlases. "Object" refers to the particular region of anatomy to be registered (e.g., head, liver, vertebra).

According to the registration basis, Fitzpatrick, *et al.* [11] classified registration techniques into three main categories: point-based methods, surface-based methods, and intensity-based methods.

(1) *Point-based*

These methods make use of a set of identified corresponding point pairs (*fiducials*) to align a given pair of views. The fiducial may be localized by interactive visual identification of anatomical landmarks. For instance, Hill *et al.*[12] combined MR and CT images for planning skull base surgery by identifying 12 to 16 homologous landmarks in each modality. Alternatively, the feature may be a marker attached to the anatomy and designed to be accurately localizable by means of an automatic algorithm [13].

(2) *Surface-based*

Surface-based methods involve determining corresponding surfaces in different images and computing the transformation that best aligns these surfaces. The skin boundary surface and the outer cranial surface are obvious choices that have frequently been used for both image-to-image (e.g., CT-MR, serial MR) and image-to-physical registration of head images. Generally, the surface representation can be simply a point set (i.e., a collection of points on the surface), a faceted surface (e.g.

triangle set), an implicit surface, or a parametric surface (e.g., B-spline surface). For all surface-based registration algorithms, the transformation must be established to minimize the disparity function. Besl and McMay [14] presented iterative closest point (ICP) method, where two surfaces assumed to be in close proximity to full alignment are registered by iteratively minimizing the sum of squared distances between mutually closest points on both surfaces.

(3) *Intensity-based*

Intensity-based methods involve calculating a transformation between two images using the pixel or voxel values alone. In their purest form, the registration transformation is determined by iteratively optimizing some "similarity measure", such as correlation coefficient, joint histograms and joint probability distributions [15], and mutual information [16,17].

2.2 Geometrical Transformations

Each view that is involved in a registration will be referred to a coordinate system, which defines a space for that view. Therefore, image registration is based on geometrical transformations, which are mappings of points from the space X of one view to that space Y of a second view. The transformation T applied to a point in X represented by the column vector $\mathbf{x}$ produces a transformed point $\mathbf{x}'$,

$$\mathbf{x}' = \mathsf{T}(\mathbf{x}).$$

If the point $\mathbf{y}$ in Y corresponds to $\mathbf{x}$, then a successful registration will make $\mathbf{x}'$ equal, or approximately equal, to $\mathbf{y}$. Any nonzero displacement $\mathsf{T}(\mathbf{x}) - \mathbf{y}$ is a

registration error. The set of all possible T may be partitioned into rigid and nonrigid transformations.

2.2.1 Rigid Transformation

Rigid transformations, or rigid mappings, are defined as geometrical transformations that preserve all distances. These transformations also preserve the straightness of lines (and the planarity of surfaces) and all nonzero angles between straight lines. Registration problems that are limited to rigid transformations are called rigid registration problems. Rigid transformations are simple to specify, and there are several methods of doing so. In each method, there are two components to the specification, a translation and a rotation. The translation is a 3D vector $\mathbf{t}$ that may be specified by giving its three coordinates t_x, t_y, t_z relative to a set of x, y, z Cartesian axes or by giving its length and two angles to specify its direction in polar spherical coordinates. There are many ways of specifying the rotational component, among them Euler angles, Cayley-Klein parameters, quaternions, axis and angles, and orthogonal matrices.

2.2.2 Nonrigid Transformation

Nonrigid transformations are important not only for applications to nonrigid anatomy, but also for interpatient registration of rigid anatomy and intrapatient registration of rigid anatomy when there are nonrigid distortions in the image acquisition procedure. They can be further divided into many subsets, such as: scaling, affine, projective, perspective, and curved transformations. In all cases, it is preferable to choose transformations that have physical meaning, but in some cases, the choice is made on the basis of convenient mathematical properties.

2.3 3D-2D Registration

Our research project aims to register 3D facial and dental models from the multimodal images – 3D dental casts, lateral cephalogram and 3D facial models – that are generated by different scanners. Both 3D images only contain the surface data and there is no direct common information between them; thus the 2D lateral cephalogram is used as a bridge relating them to each other. There are two main parts to be implemented: one is the registration of the facial model and the lateral cephalogram, the other is that of the dental cast and the lateral cephalogram. Thus, the complex 3D-3D multimodality image registration can be solved through 3D-2D image registration.

3D-2D registration (as well as 2D-3D) is the process of trying to align a 2D view of an object with the 3D data of an object. To solve this problem, Feldmar *et al.* [18] introduced three different techniques depending on the particular clinical problem.

(1) *3D-2D curve-based*

The objects are represented as curves described by points and associated tangents in both the 3D and the 2D images. Hence, from a computer vision point of view, the problem is to find the best projective transformation that maps a given 3D curve onto a given 2D curve.

(2) *3D-3D surface-based*

These methods aim to find the correspondence between a 3D image and the actual position of the patient. Generally, passive stereo is used to reconstruct a 3D surface during the intervention; the result is a dense description using points and normals of the patient's surface. Subsequently, the problem is to find the transformation between the 3D image (e.g., MRI, CT) and the reconstructed surface.

(3) *3D-2D surface-based*

3D-2D surface-based methods aim to find the transformation between a 3D surface and an image of the surface by using the silhouette. That is to say, the position of the 3D pre-operative object is determined such that its projection corresponds to the occluding contours detected in the 2D intra-operative image.

Cyr *et al.* [19] also described a shape-based registration method for 2D-3D registration of 3D volumetric images such as CT an MR, and 2D projection images such as X-ray and fluoroscopic images. The method is mainly based on a sampling of the viewing sphere and matching the given 2D view with the series of projected shapes to determine the best view.

The above mentioned 3D-2D registration techniques have shown excellent results in certain areas. However, to solve our specific problem, we propose a facial profile-based technique in Chapter 3 to register the 3D facial model and 2D lateral X-ray cephalogram, which is different from the methods mentioned above in the following aspects. (a) For the pose estimation of facial model, the nose ridge is used as a search cue, which is much faster than the shape-based methods discussed in [8]. (b) The facial profiles are extracted from 3D facial model and lateral X-ray cephalogram separately, and the geometrical transformation is calculated based on these two facial profiles. Hence, the 3D-2D registration problem is actually simplified to a 2D-2D curve registration problem.

As for the registration between 2D lateral X-ray cephalogram and 3D dental casts discussed in Chapter 4, several landmarks are used to determine the correct geometric transformation. Finally, the integrated dentofacial image provides 3D coordinate data,

which is applicable to quantitative analysis research. Figure 2.1 shows the entire framework of the proposed dentofacial registration system.

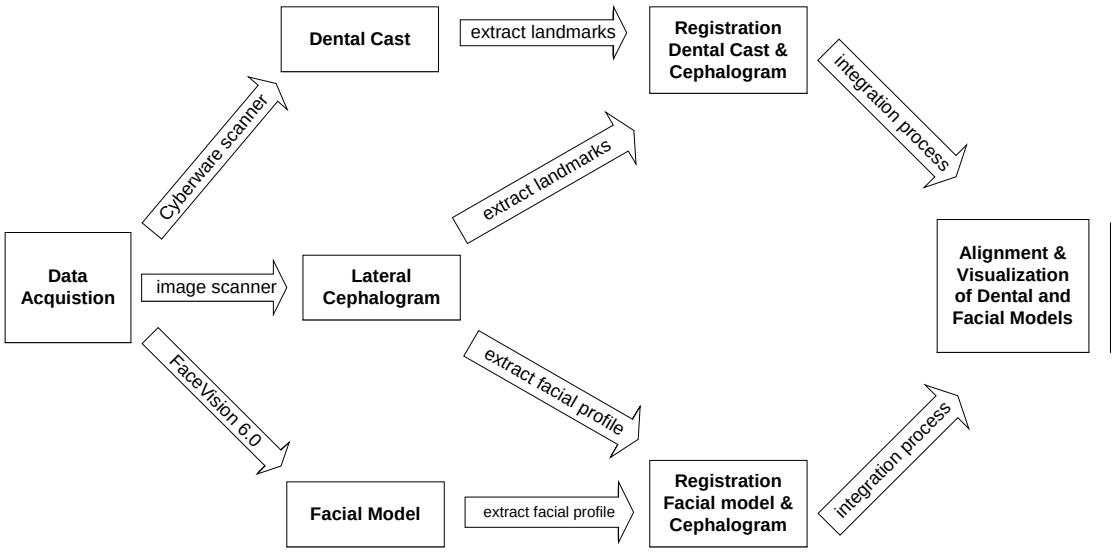

Figure 2.1: Framework of 3D dentofacial registration system

Chapter 3 Facial Model – Cephalogram Registration

The purpose of our project is to register the 3D dental cast with the 3D facial shape model. However, there is no direct common information between these two kinds of data as both of them only provide surface information of the corresponding 3D models. This is the reason why 2D cephalogram images are involved in our project. For the sake of simplicity, only lateral cephalogram images are used to assist the 3D registration. Since, the facial profile is a good way to relate the 2D lateral cephalogram image to the 3D facial model, facial profile analysis is also indispensable.

3.1 Facial Profile Analysis: Literature Review

For the extracted facial profile of a face, it is important to identify facial profile fiducials that may be used for image registration. Figure 3.1 shows a facial profile along with the eleven fiducials that are considered most significant [20]. The identification of fiducials along the profile of the human face has several important applications, e.g., in the fields of medical imaging, face recognition, and anthropology.

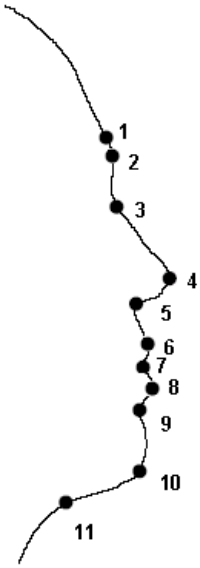

Figure 3.1: The eleven facial profile fiducials that are most often used in facial profile analysis [20]. The fiducials are numbered from top to bottom: (1) forehead, (2) glabella, (3) nasion, (4) pronasale, (5) subnasale, (6) labiale superius, (7) stomion, (8) labiale inferius, (9) supramenton, (10) menton, and (11) throat.

Facial profile analysis has been an active area of research for over a century; however, there is still no single technique that can reliably extract all of the salient fiducials for every face. This is not surprising, because there are so many variations of “normal” facial profiles. Generally, conventional and automated facial analysis techniques can be grouped into three main approaches: tangent-based, where lines tangent to the profile are used to locate fiducials relative to other fiducials; curvature-based, where the curvature of the profile is used to locate ficucials as points of maximal absolute curvature; and template matching, where a template is mapped onto the profile and fiducials are extracted from the profile based on where pre-determined fiducials on the template get mapped.

3.1.1 Tangent-based Techniques

Tangent-based techniques rely on the assumption that by choosing the appropriate reference point, there will be a line through the reference point that is tangent to the facial profile at one of the fiducials. Harmon *et al.* [20, 21] developed the technique for extracting the eleven fiducials.

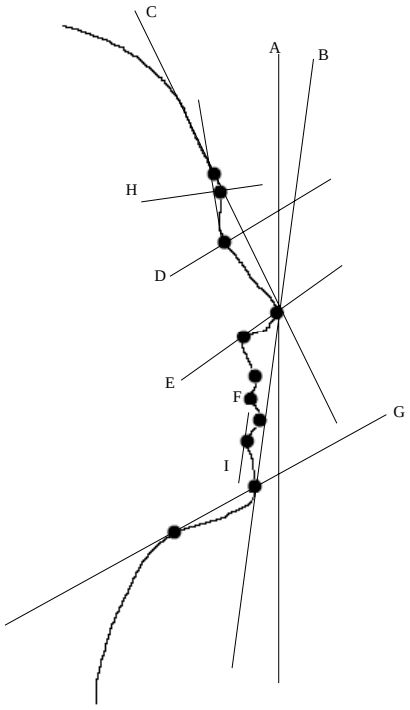

Figure 3.2: The technique that Harmon *et al.* used to extract the eleven fiducials from the profile.

Figure 3.2 illustrates the technique used by Harmon *et al.*. The most lateral point on the profile touched by the vertical line A is the approximate pronasale. Line B, which is close to the approximate pronasale and bitangent to the segment of the curve below the approximate pronasale, defines the chin and pronasale points. The forehead point is determined by line C, which is tangent to the top of the curve and passes through the pronasale. The nasion is the point on the profile between the pronasale and

forehead that is most distant (D) to the line segment from the pronasale to the forehead. The subnasale is the point on the ray (E) from the pronasale that is tangent to the interior of the profile just below the pronasale. The lips are found between the subnasale and chin based on the raduis of curvature (F). The throat is the point on the ray (G) from the chin that is tangent to the interior of the profile just below the chin. The glabella is the point on the profile between the nasion and forehead that is most distant (H) to the line segment from the nasion to the forehead. The supramenton is the innermost point (I) on the profile between the chin and bottom lip.

Okamoto *et al.* [22] used eleven fiducials that were mostly similar to those used by Harmon *et al.*, except that they employed an extra fiducial between the pronasale and subnasale, and a fiducial between the suprementon and chin.

However, the most significant problem with tangent-based techniques is that there will not be a line that is bitangent to the pronasale and chin for profiles with protruding lips. Another problem with tangent-based techniques is that an initial reference point, such as the pronasale, needs to be chosen, and the choice can be unreliable without higher order statistics such as curvature.

3.1.2 Curvature-based Techniques

Curvature-based techniques are invariant to rotation, translation, and scaling. Campos, Linney, and Moss [24] analyzed facial profiles by using scale space techniques to extract the most prominent eight fiducials. According to their approach, the curvature of each point along the profile is first calculated for a number of levels of Gaussian smoothing, producing a scale-space image of the profile (Figure 3.3). Then the zero-

crossings of the curvature are detected for each of the levels of smoothing, producing zero-crossing contours. After that, an appropriate level of smoothing is chosen by gradually reducing the amount of smoothing until there are exactly nine intersections with the zero-crossing contours. The nine zero-crossing points segment the smoothed profile into ten curve segments. The end segments are ignored and the fiducials are extracted as the points of maximal absolute curvature for each of the remaining eight segments.

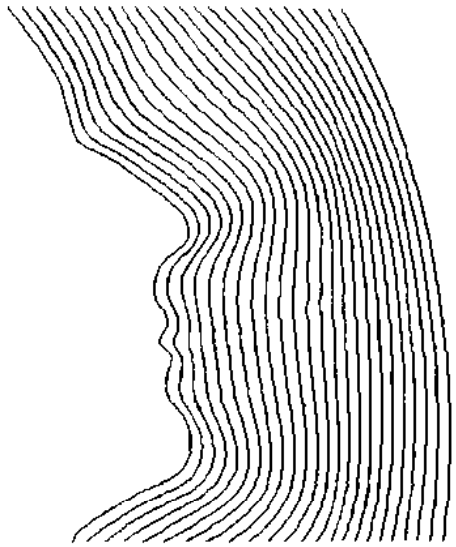

Figure 3.3: Sequence of Gaussian convolved facial profiles showing the smoothing effect [24]. The scale parameter is increasing from left to right.

Kang Dariush and Waters [23] extracted nine fiducials based on the observation of that the curvature of the profile alternates between convex and concave, with the point of maximal absolute curvature in each segment corresponding to a fiducial. In addition, Johnson and Wu [25] used curvature and fuzzy logic to choose the points on the profile corresponding to these five fiducials: nasion, pronasale, subnasale, stomion, and chin.

3.1.3 Template Matching Techniques

Suenaga Akimoto, and Wallace [26] used a template matching approach to find the position of the same five fiducials used by Johnson and Wu [25]. The template, consisting of approximately 50 line segments to represent a generic facial profile, is fitted to the profile by finding a set of points that minimize a cost function. The matching produces a mapping from each point in the template to a point on the profile. Five fiducials are defined on the template, so that the corresponding points on the profile are the detected fiducials.

In our research project, the facial profile analysis plays an important role in the registration of 3D facial model and 2D cephalogram image. Comparing the three techniques mentioned above, we find that curvature-based techniques are more suitable for registration due to the following reasons:

(1) They are invariant to rotation, translation, and scaling.

(2) They overcome the limitations of tangent-based techniques, and are more accurate.

(3) They are much easier and faster to implement than template matching techniques.

3.2 Facial Profile Extraction in X-rays

One of the X-rays of the samples is shown in Figure 3.4a. It was taken by a computed radiograph unit, and printed on acetate film. No further details about the underlying image geometry are known. We will assume that it was obtained by a parallel projection. Then the image was scanned to a digital format using Agfa's ARCUS II

Scanner [27] and Fotolook 2.08β Standalone Software running under Windows NT. During the course of the scanning, the image contrast is adjusted by varying the γ value. Generally speaking, the larger the value of γ, the more visible the soft tissue would be, but more detailed information will be lost in hard tissue (image becomes too white). Therefore by adjusting γ, we attempt to make the soft tissue visible, without losing the details in the hard tissue. After obtaining the digitized cephalogram image, we can process it to extract the facial profile.

3.2.1 Preprocessing of X-rays Images

The aim of preprocessing is to enhance images to be suitable for further analysis. Here, preprocessing enhances the soft tissue prior to the facial profile extraction.

Figure 3.4 shows the entire process of image preprocessing in the X-ray image. Median filtering is first used to reduce any noise (Figure 3.4b) that might be introduced by scanning. Global histogram equalization is applied to improve the contrast, and make the distribution of gray value uniform (Figure 3.4c). Because the soft tissue is much darker than the hard tissue in the X-ray image, we use logarithm filtering to enhance the dark areas where the information about the soft tissue may exist, that is, the soft tissue facial profile is enhanced for easier extraction (Figure 3.4d).

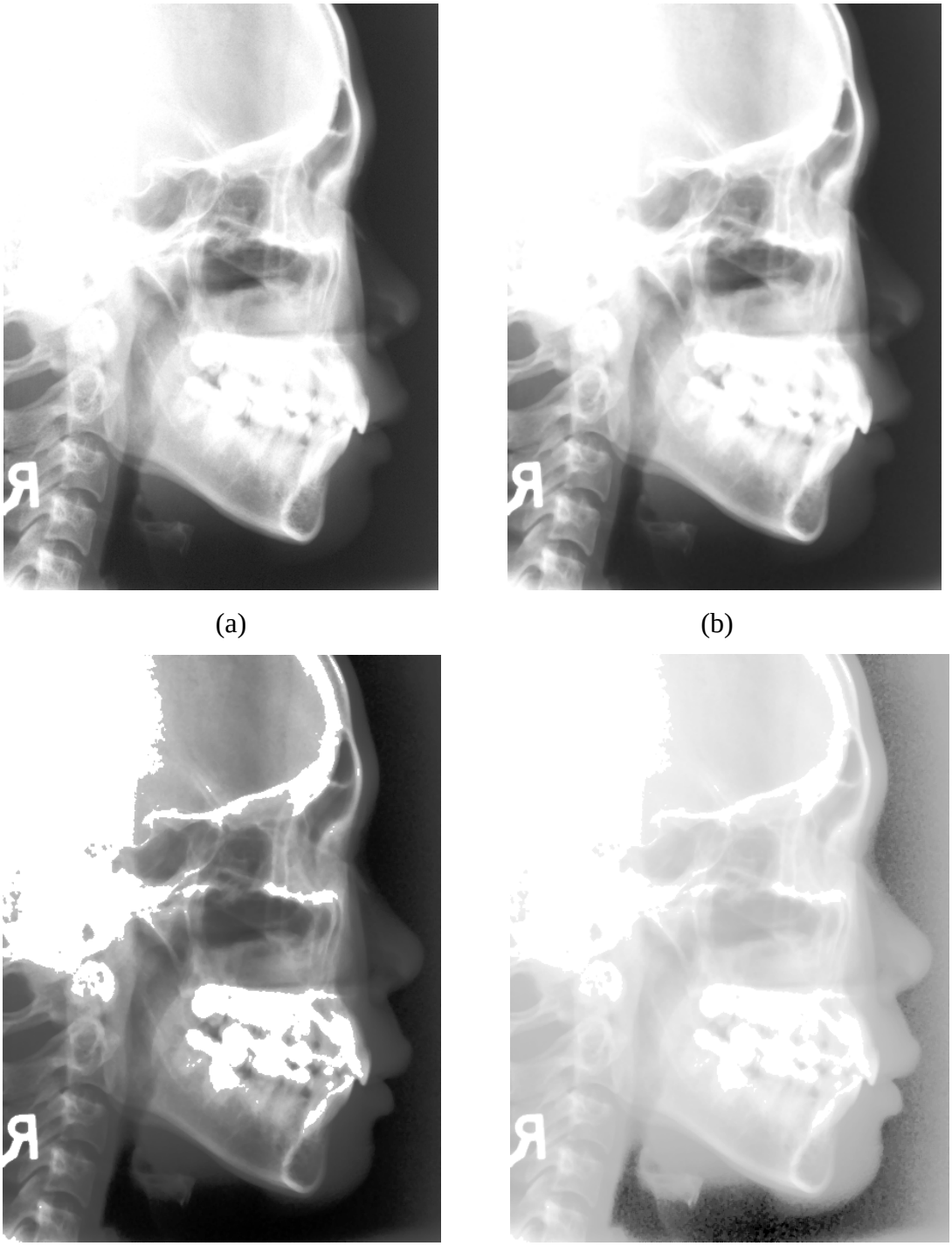

(a) (b)

(c) (d)

Figure 3.4: Image preprocessing in the cephalogram. (a) Original cephaologram, (b) After median filtering, (c) After histogram equalization, and (d) After logarithm filtering.

3.2.2 Edge Detection

Edge detection is a fundamental problem in image processing. There is a wide range of papers in the subject on edge detection filters and the algorithms that work with various degrees of success for different images. A good selection of references is given in [28]. An optimal edge detector should be characterized by good signal to noise ratio (S), good locality (L), and maximum suppression of false responses (C). Compared with the Canny [29] and Spacek [30] filters, we found that Petrou and Kittler's edge detectors [31] perform best for extracting edges in the X-rays.

Petrou and Kittler argued that, in developing an optimal filter, an edge should be modeled as an ideal edge that has undergone low pass filtering with noise addition. They considered the unrealistic omission of the low pass filter in Canny's and Spacek's approaches. Another difference is that Petrou and Kittler's filter is designed to maximize the total performance measure $(SLC)^2$, for ramp edges of various slopes; while what Canny did was to maximize SL . Furthermore, the Gaussian filter is used to obtain the smoothed image in the practical implementation of the Canny filter. The Gaussian filter works well when the edges are more like step edges, but it is unrealistic to expect image edges to be step-like. The performance of the Gaussian filter varies significantly according to the value of the standard deviation chosen.

More importantly, Petrou and Kittler provided other researchers with some convolution masks which can be used directly during edge detection without the need to go into the details of the subject. The steps of such a method is described briefly as follows.

Firstly, the preprocessed image obtained above is smoothed using the 11×11 convolution mask for ramp edges suggested by Petrou and Kittler.

Secondly, the Prewitt operator performs 2D spatial gradient measurement on the smoothed image. Then, the approximate absolute gradient magnitude (edge strength) at each point can be found. The Prewitt operator uses a pair of 3×3 convolution masks, one estimating the gradient in the $x-$direction and the other estimating the gradient in the $y-$direction. The magnitude of the gradient and the edge direction are then approximated by

$$|G| = \sqrt{(G_x)^2 + (G_y)^2}\ , \tag{3.1}$$

$$\alpha = \tan^{-1}\left(G_y \big/ G_x\right). \tag{3.2}$$

Finally, nonmaximum suppression is applied to suppress any pixel value (setting it equal to 0) that is not considered to be an edge, and to thin wide edges to one-pixel. Figure 3.5 shows the edges that are successfully extracted by implementing Petrou and Kittler's method.

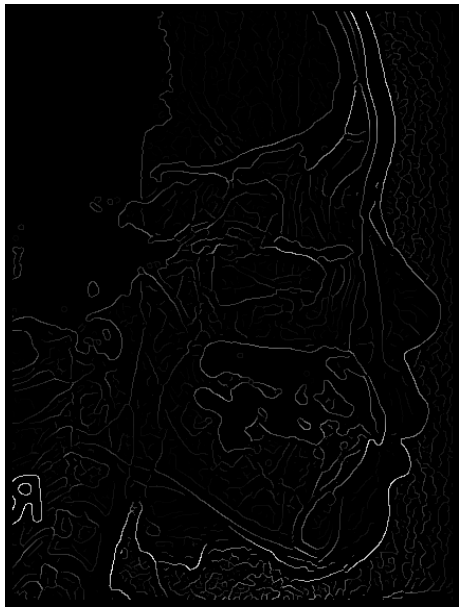

Figure 3.5: Petrou and Kittler's edge detector.

3.2.3 Facial Profile Extraction

Following the above process, the image thresholding method proposed by Ostu [32] is applied, and the binary image obtained is shown in Figure 3.6a. There are many small objects in that image, so they are removed according to the segment length (Figure 3.6b). Finally, the facial profile is traced continuously within 8-connected neighbors, and segmented out as the longest curve in the rightmost side of the image (Figure 3.6c). In order to see the performance of edge detector we use, the facial profile extracted is superimposed onto the original X-ray, as shown in Figure 3.6d.

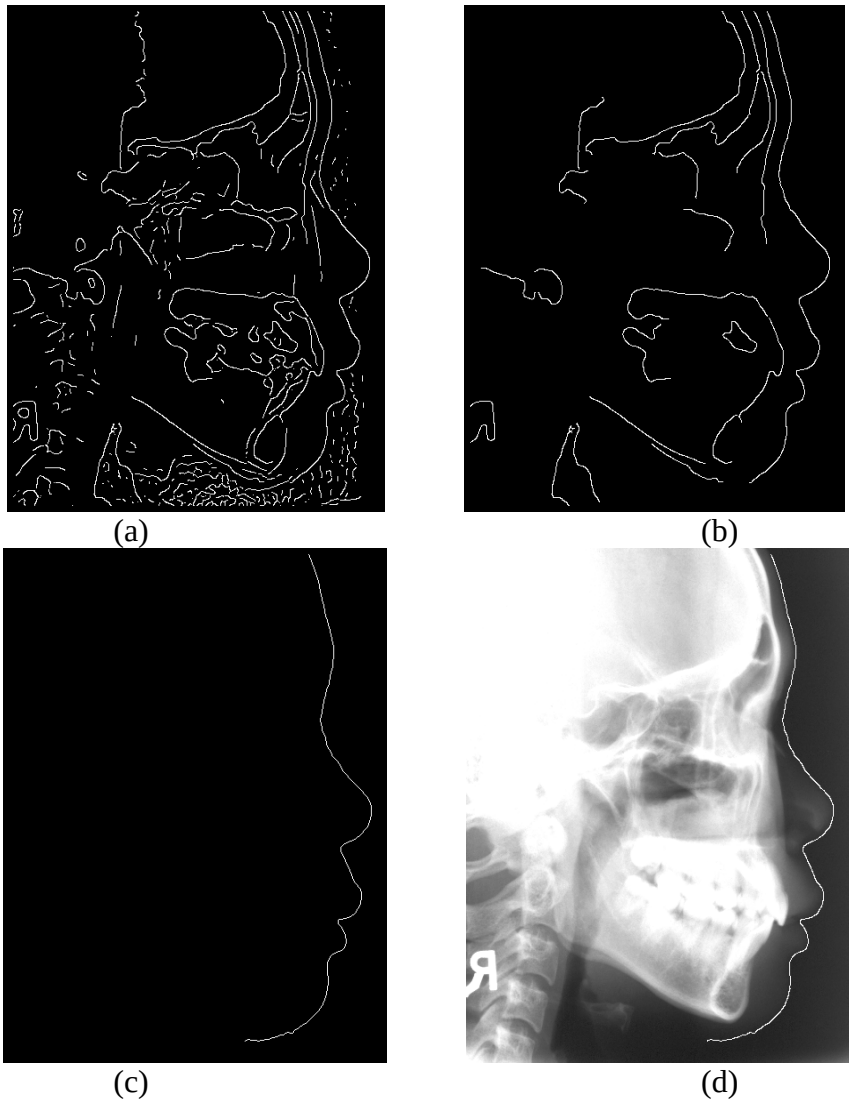

Figure 3.6: Facial profile extraction. (a) Apply image thresholding, (b) Remove small objects, (c) Trace facial profile, and (d) Superimpose the facial profile on X-ray.

3.3 Facial Profile Extraction on Facial Model

3.3.1 The Visualization of 3D Facial Model

3D facial model is obtained by scanning a subject or patient using a *FaceVision* scanner (Geometrix Inc.). The output data is exported as *VRML* format, which is visualized as shown in Figure 3.7a. The texture information (Figure 3.7b) can be mapped onto the 3D facial model, and the result is shown in Figure 3.6c.

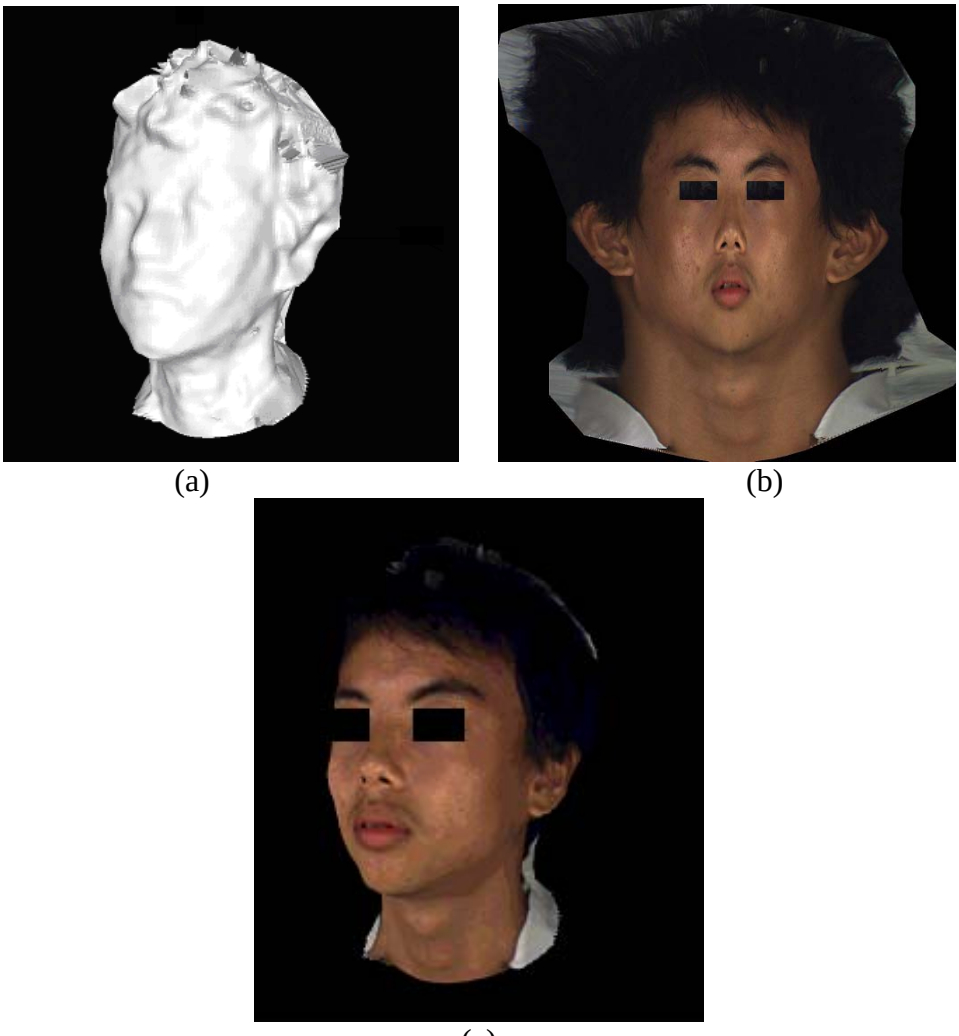

(a) (b)

(c)

Figure 3.7: 3D facial model scanned by *Facevision* scanner. (a) Facial model without texture mapping, (b) Texture information, and (c) Facial model with texture mapping.

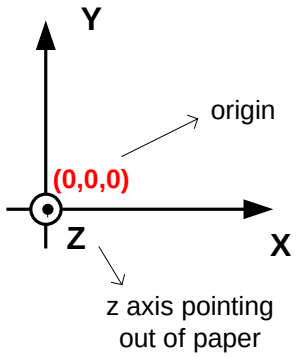

Figure 3.8: Coordinate systems of 3D world

During visualization, the world coordinate system is consistent with the right hand rule as shown in Figure 3.8. The centroid $(\bar{x}, \bar{y}, \bar{z})$ of the head is translated to the origin $(0,0,0)$ of the coordinate system, with the $y-$axis corresponding to height, the $x-$axis corresponding to the left and right of the head, and the $z-$axis corresponding to the front and back of the head. Here, the centroid $(\bar{x}, \bar{y}, \bar{z})$ is defined by

$$\bar{x} = \frac{1}{M}\sum_{i=1}^{M} x_i \tag{3.3}$$

$$\bar{y} = \frac{1}{M}\sum_{i=1}^{M} y_i \tag{3.4}$$

$$\bar{z} = \frac{1}{M}\sum_{i=1}^{M} z_i \tag{3.5}$$

where (x_i, y_i, z_i) are the coordinates of vertex i and m is the number of vertices on the scanned facial model.

3.3.2 Facial Profile Extraction

The method to extract the facial profile from the 3D facial model is based on detecting the ridge of the nose in cross-sections of the head. The ridge points are then used to estimate the vertical plane, passing through the centroid of the head, that most closely intersects the ridge of the nose. Figure 3.9 illustrates the process of profile extraction on 3D facial model. First, the cross-sections (Figure 3.9b) are converted from Cartesian coordinates to polar coordinates (Figure 3.9c) and analyzed to detect the nose ridge points (marked by circles in Figure 3.9d). Then, the angles required to rotate the model are calculated. The result is an aligned 3D facial model with the line of best fit for the nose ridge on the xy plane (Figure 3.9e). Finally, a 2D facial profile (Figure 3.9f) is extracted from the aligned 3D facial model.

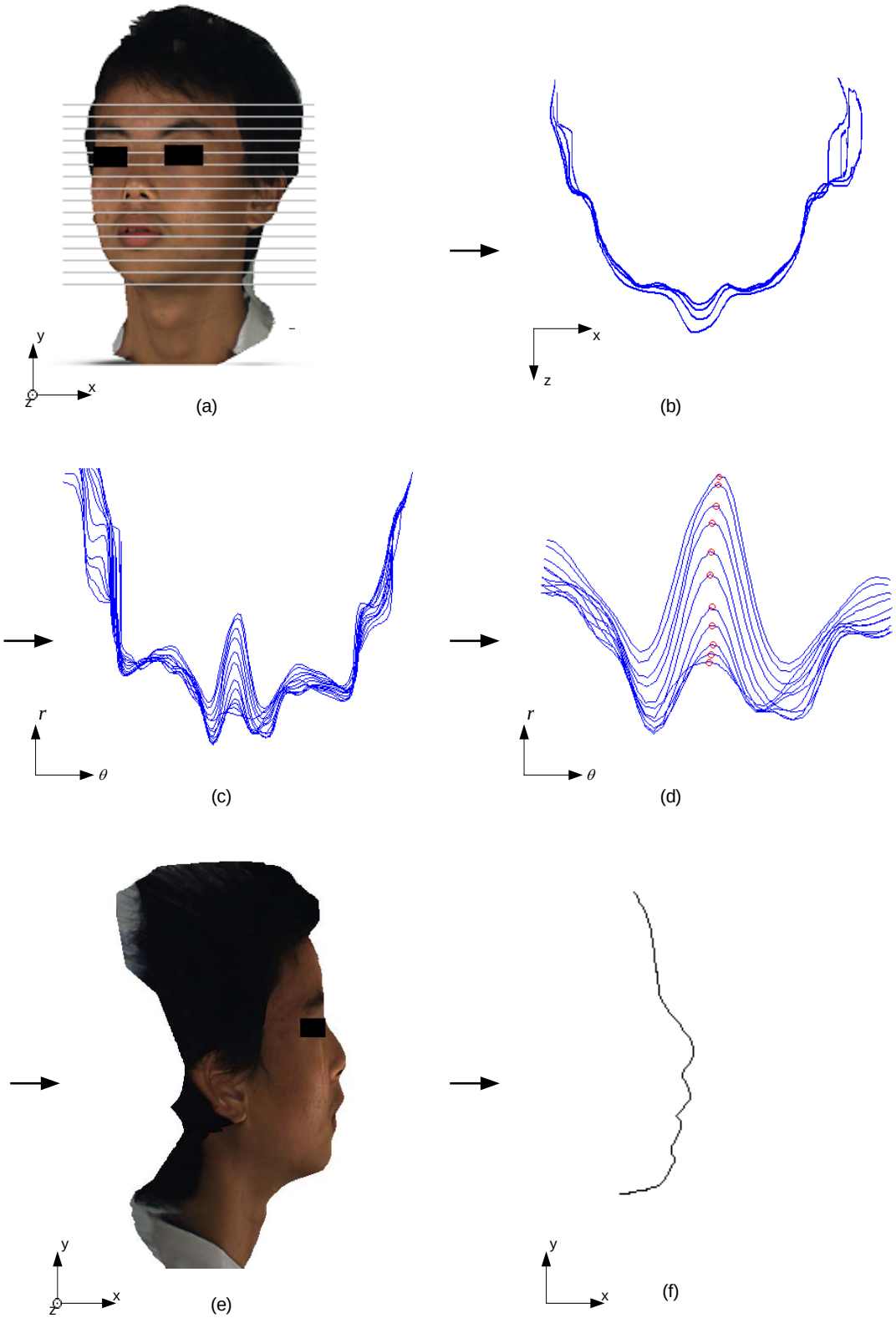

Figure 3.9: Process of profile extraction from 3D facial model. (a) Facial model, (b) Cross-sections in Cartesian coordinates, (c) Cross-sections in polar coordinates, (d) Cross-sections with nose-ridge points, (e) Aligned facial model, and (f) Facial profile extracted from the facial model.

3.3.2.1 Nose ridge detection

The first step is to extract 2D cross-sections across the head at 2 mm intervals by calculating the intersection of the head surface with the planes defined by $y = y_i$, where y_i is the distance from the origin $(0,0,0)$ to the i^{th} plane, i is from 0 to 30. Figure 3.10 shows a typical cross-section containing the ridge of the nose.

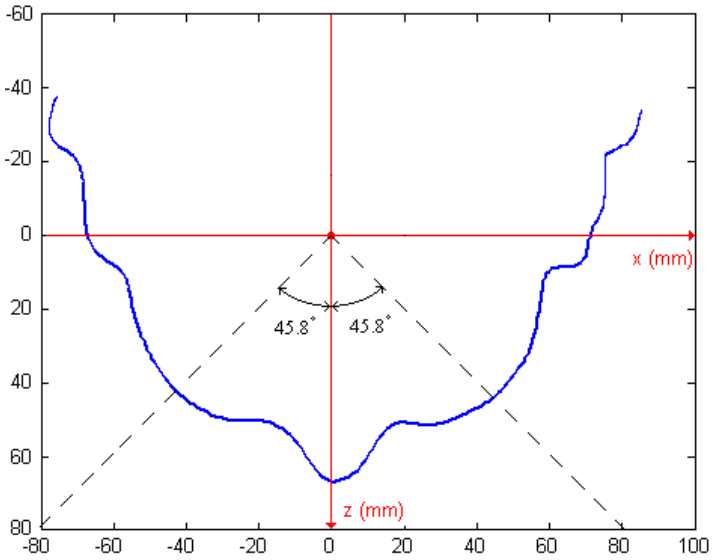

Figure 3.10: A cross-section in Cartesian coordinates.

The cross-sections are rotated anticlockwise by 90° to place the nose near $x-$axis, then converted from Cartesian to polar coordinates. Since the nose is near the angle zero in polar coordinates, all data points farther than 0.8 rad (45.8°) away from the xy plane are discarded, that is, the back and sides of the head are ignored. The equations to convert the point (x,z) from Cartesian coordinates to the point (r,θ) in polar coordinates are

$$r = \sqrt{x^2 + y^2} \tag{3.6}$$

and

$$\theta = \arctan\left(\frac{z}{x}\right). \tag{3.7}$$

The cross-sections that are above or below the nose contain useless information for nose bridge detection, therefore they should be discarded. Such cross-sections can be detected easily. If the initial position of the nose is very near the angle zero in polar coordinates, there should be a peak near 0 rad along the profile as shown in Figure 3.11. If there does not exist a peak, the corresponding cross-section is discarded.

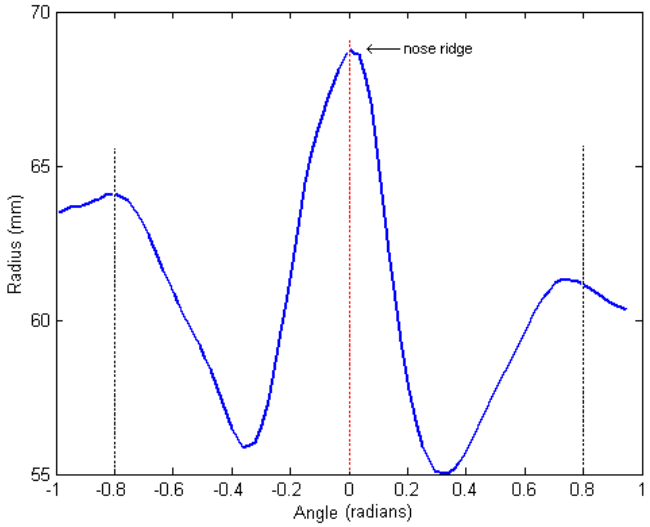

Figure 3.11: A cross-section in polar coordinates.

The following step is to detect the nose-ridge points in the profile of each cross-section in polar coordinates. The nose-ridge points are local maximal points in the polar plot. Since measurement errors can appear in the data, which are typically caused by the movement of the person during imaging, a Gaussian filter is used to smooth the cross-sections in polar coordinates. Supposed the cross-section is

$$\Gamma = \{r(\theta) \mid \theta \in [-0.8, 0.8]\}, \tag{3.8}$$

Let $g(u, \sigma)$ denote a 1D Gaussian of width σ defined by:

$$g(u,\sigma)=\frac{1}{\sigma\sqrt{2\pi}}e^{\frac{u^2}{2\sigma^2}}, \tag{3.9}$$

Then the smoothed cross-section Γ_σ is:

$$\Gamma_\sigma = \Gamma * g(u,\sigma). \tag{3.10}$$

where $*$ denotes convolution.

Suitable values of the parameters were obtained experimentally. Since a large filter size results in the loss of the detail in the edges, we set the parameter u within the moderate range of –2 to +2. At the same time, the parameter σ was increased until the Gaussian smoothing filter can filter out the spurious points that may influence the detection of local maximum. For the specific problem in our project, the following parameter values were used:

$$\sigma = 0.93,$$

$$-2 \le u \le +2.$$

And the smoothed result is shown in Figure 3.12.

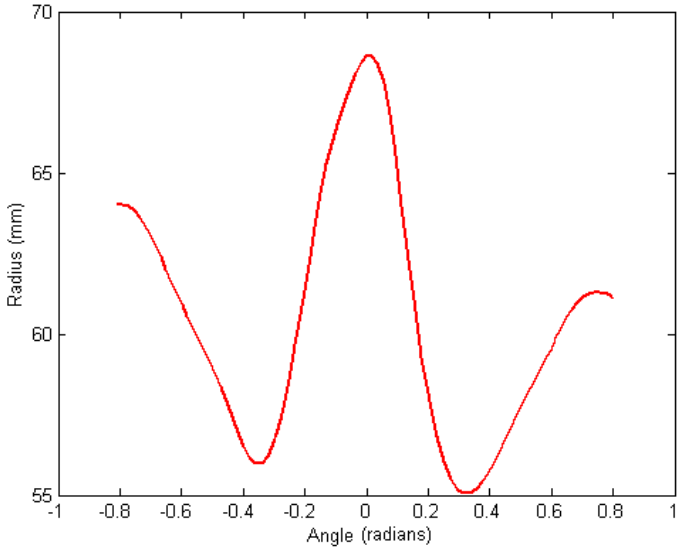

Figure 3.12: A smoothed cross-section.

Finally, the Cartesian coordinates for the detected ridge points are recorded. The set of n ridge points gives the nose-ridge P:

$$\mathrm{P} = \{(x_1, y_1, z_1), (x_2, y_2, z_2), \cdots, (x_n, y_n, z_n)\},$$

where $(x_i, y_i, z_i),\ 1 \le i \le n$ indicates the 3D coordinates of the i^{th} ridge point, and the points are ordered by their z coordinates.

The above proposed method performs well for nose ridge detection when the head is upright. However, if the subject tilts his head (Figure 3.13), this method may not detect enough nose-ridge points for the following step of facial model alignment. And the further the head is tilted, the more difficult it is to detect nose-ridge points. Figure 3.14 illustrates the reason why the method fails to detect the nose ridge points. Figure 3.14a shows a cross-section of the tilted head in Cartesian coordinates and the position of nose bridge can be identified. Unfortunately, after it is converted into polar coordinates (Figure 3.14b), there does not exist a peak indicating the nose ridge, and if any peak exists near 0 rad, it would indicate the cheek, not the nose bridge.

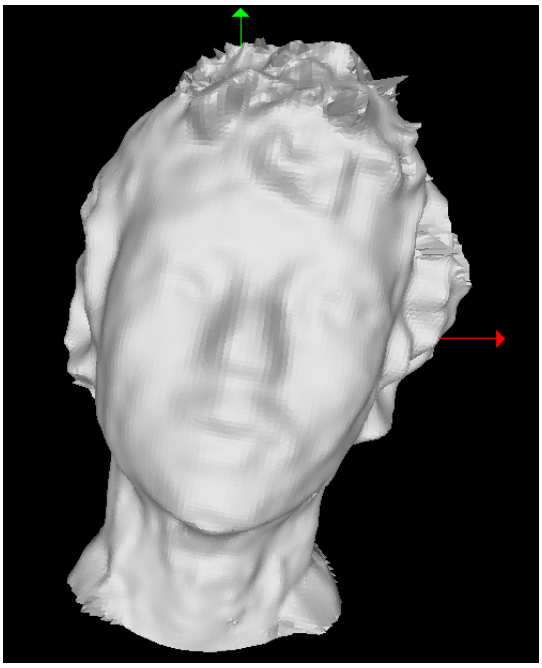

Figure 3.13: The head tilted by 10° to the right.

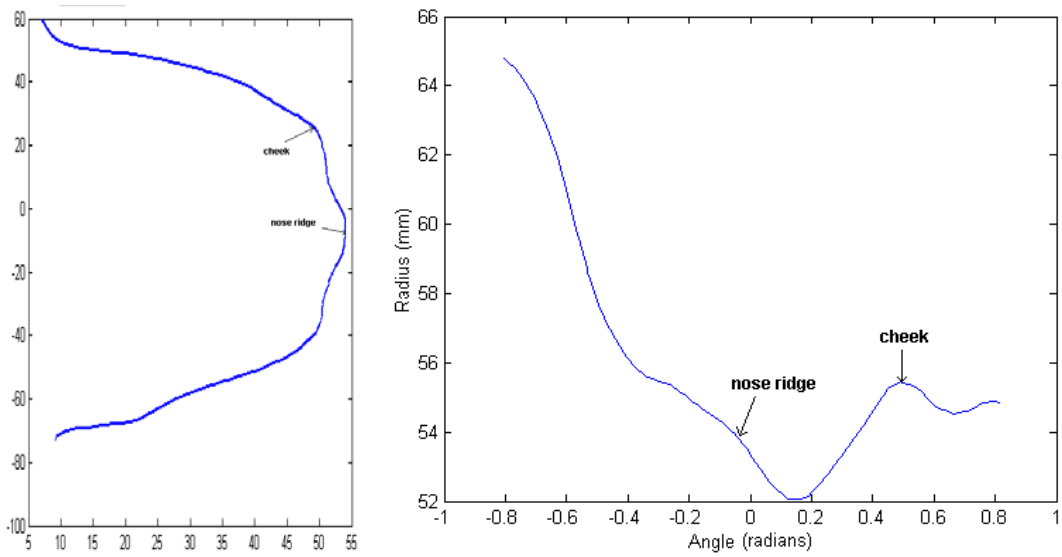

(a) (b)

Figure 3.14: A cross-section of the head tilted to right 10°. (a) In Cartesian coordinates. (b) In polar coordinates.

In our project, the subject is asked to keep the eyes within the two horizontal lines during taking the scanning to meet the requirement of the *FaceVision* scanner. This requirement guarantees that the subject's head is not tilted too much (<5°). Hence, most of the nose ridge points of the cross-sections can be detected successfully by using the proposed method.

3.3.2.2 Facial model alignment

Now that a set of 3D points corresponding to the ridge of the nose has been detected, the data for the facial model can be aligned so that the nose ridge is on the *xy* plane. The following diagram illustrates the process.

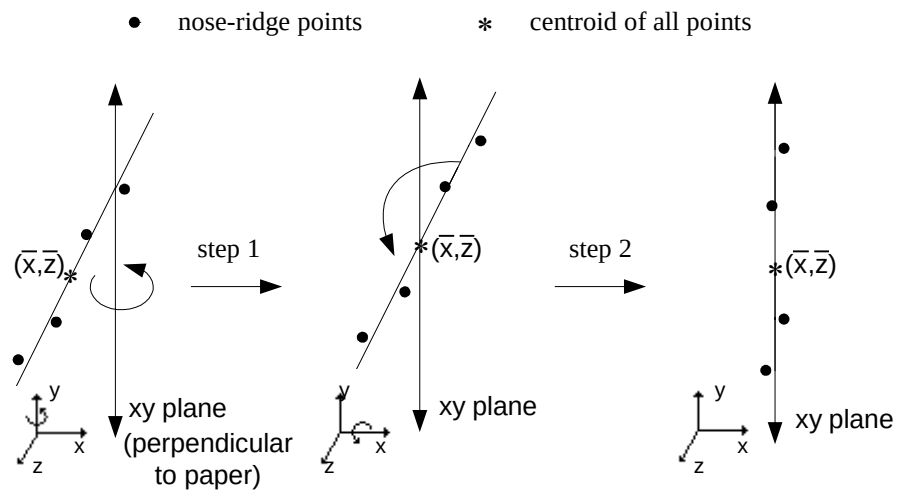

Figure 3.15: This diagram illustrates how to rotate the ridge points onto the *xy* plane.

The first step in alignment of the data is to rotate about the *y* axis, so that the centroid of the ridge points is on the *xy* plane. This is achieved by projecting the nose-ridge points in P onto the *xz* plane and discarding the *y* coordinate to produce the set of 2D ridge points P_1

$$P_1 = \{(x_1, z_1), (x_2, z_2), \cdots, (x_n, z_n)\}.$$

$(\bar{x}, \bar{z})$ is defined as the mean 2D ridge point, where

$$\bar{x} = \frac{1}{n}\sum_{i=1}^{n} x_i \,, \tag{3.11}$$

and

$$\bar{z} = \frac{1}{n}\sum_{i=1}^{n} z_i \,. \tag{3.12}$$

It can be seen from Figure 3.16 that the angle of rotation about the *y* axis is $\arctan(\bar{z}/\bar{x})$ to rotate $(\bar{x}, \bar{z})$ onto the *xy* plane. The ridge points, P_1, are then rotated about the *y* axis by this angle to produce the set of ridge points P_2

$$P_2 = \{(x_1', y_1', z_1'), (x_2', y_2', z_2'), \cdots, (x_n', y_n', z_n')\}.$$

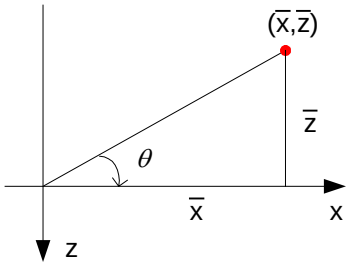

Figure 3.16: Rotating $(\bar{x}, \bar{z})$ onto the xy plane.

Thus the centroid of P_2 is on the xy plane, but the ridge may not be on this plane. To ensure the entire nose ridge is on the xy plane, the rotated ridge points are projected onto the yz plane by discarding the x coordinates to produce the set of 2D ridge points P_3

$$P_3 = \left\{\left(y_1^{'}, z_1^{'}\right), \left(y_2^{'}, z_2^{'}\right), \cdots, \left(y_n^{'}, z_n^{'}\right)\right\}.$$

These ridge points are unlikely to lie in a perfectly straight line, so that linear regression is performed to determine the line of best fit. The equation for this line is

$$y^{'} - \bar{y}^{'} = b(z^{'} - \bar{z}^{'}), \tag{3.13}$$

where the mean coordinate, y, for the set P_3 is

$$\bar{y}^{'} = \frac{1}{n}\sum_{i=1}^{n} y_i^{'}, \tag{3.14}$$

the mean coordinate, z, is

$$\bar{z}^{'} = \frac{1}{n}\sum_{i=1}^{n} z_i^{'}, \tag{3.15}$$

and the slope, b, is defined as the sample covariance of $y^{'}z^{'}$ divided by the sample variance of $y^{'}$

$$b = \frac{s_{y^{'}z^{'}}}{s_{y^{'}}^2}, \tag{3.16}$$

where

$$s_{y'z'} = \frac{1}{n-1}\sum_{i=1}^{n}\left(z_i' - \bar{z}'\right)\left(y_i' - \bar{y}'\right), \tag{3.17}$$

and

$$s_{y'}^2 = \frac{1}{n-1}\sum_{i=1}^{n}\left(y_i' - \bar{y}'\right)^2 . \tag{3.18}$$

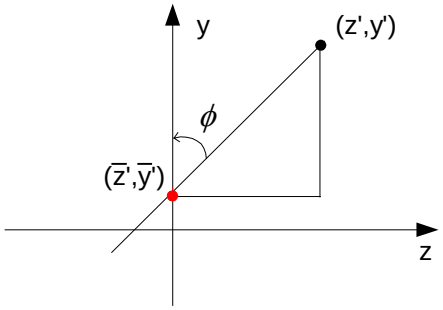

Figure 3.17: Rotating the nose-ridge points to the xy plane.

If the sample variance of y' is zero, then the line of best fit for the nose-ridge points is already in the vertical plane, thus no rotation is required. It can be seen from the diagram in Figure 3.17 that the angle of rotation about the *x* axis, with the rotation centred at the centroid of the nose-ridge points, is $-\phi$, where $\phi = \arctan(1/b)$.

3.3.2.3 Facial profile extraction

After the 3D facial model has been aligned, the nose ridge lies on the xy plane, and a 2D facial profile can be extracted from the 3D surface data. The extraction process is described as follows.

The surface of the facial model is a triangulated mesh. Every little triangle in the mesh is tested for intersection with the *xy* plane. In order to save processing time, each triangle is validated first. If the three vertices of a triangle lie on the same side of the xy plane, this triangle is invalid, and there is no need to calculate its intersection with the *xy* plane. For each valid triangle, two sides intersect with the plane. The line segment joining point (x_1, y_1, z_1) and point (x_2, y_2, z_2) can be described using the parametric equation

$$(x, y, z) = (x_1, y_1, z_1) + t((x_2 - x_1), (y_2 - y_1), (z_2, z_1)), \qquad (3.19)$$

where *t* is a real number, and the line segment joining (x_1, y_1, z_1) and (x_2, y_2, z_2) is defined by $0 \le t \le 1$. Then solving the parametric equation for the line segment when $x = 0$ yields the value for *t*:

$$t = \frac{z_1}{z_1 - z_2},$$

when $z_1 \neq z_2$. If $z_1 = z_2$, the line segment is on the plane, so all values of t produce a point that is on the plane, as well as on the sides of triangles. So the value of *t* is substituted into Equation (3.19) to calculate the point of intersection. The *x* and *y* axes form a basis for the plane $z = 0$, so the *z* coordinate can be discarded to reduce the dimensionality of the point from three dimensions to two dimensions.

After all points of intersection between triangles in mesh and the xy plane have been calculated, the points are then connected by joining the point with the lowest *y* coordinate to its nearest neighbor, and then join that point to its nearest neighbor, and so on until all intersection points have been connected. The result is an ordered set of 2D points

$$\text{FP} = \{p_1, p_2, \cdots, p_n\},$$

where FP represents the extracted facial profile, and $p_k = (y_k, z_k)$ is connected to $p_{k+1}(y_{k+1}, z_{k+1})$. Figure 3.18 shows the extracted 2D profile from the 3D facial model.

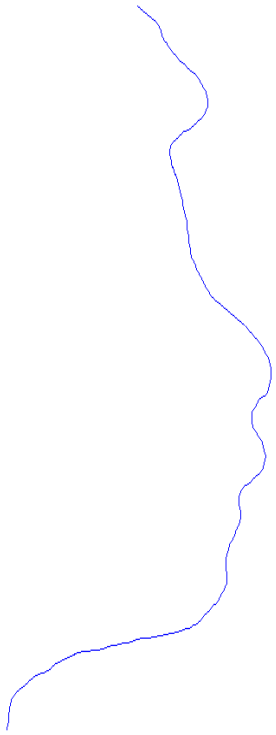

Figure 3.18: Facial profile extracted on 3D head.

3.4 Registration Between Facial Profiles

To register facial profiles, the analysis of facial profiles is helpful. Three categories of techniques have been reviewed in Section 3.1, namely tangent-based, curvature-based, and template matching. For a curve, an interesting feature is its curvature (the inverse of the local radius) because it is shift and rotation invariant and it allows for the detection of relevant reference points (local maxima). Hence, we propose a method, which is an improved curvature-based method, to extract the fiducial points

along the facial profiles. Then the geometrical transformation is calculated by using singular value decomposition (SVD) [33] as described in Appendix A.

3.4.1 Initial Position Estimation of Fiducials

The novelty of the improved curvature-based method lies in the method of estimation of the initial position of each fiducial. The distance from any point on the facial profile to the baseline is calculated as shown in Figure 3.19. Then the points at a local maximum or minimum are regarded as the initial positions of the fiducials.

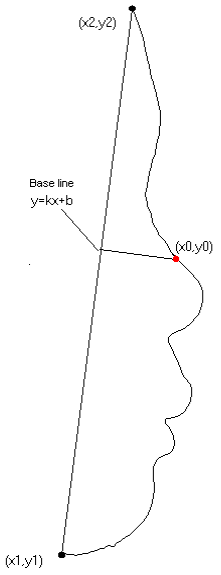

Figure 3.19: Calculating the distance from a point on the profile to the base line.

Supposing the base line is defined by

$$y = kx + b, \tag{3.20}$$

the distance from any point (x_i, y_i) on the profile to the line is

$$D_i^{\,2} = \frac{|kx_i + b - y_i|}{\sqrt{1+k^2}}. \tag{3.21}$$

A “distance plot” is drawn as shown in Figure 3.20. A linear Gaussian filter is used to smooth the “distance plot”, and the result is shown in Figure 3.21. After that, the initial position of each fiducial point can be identified as the local maxima and minima, and marked by $P1, P2, \cdots, P9$.

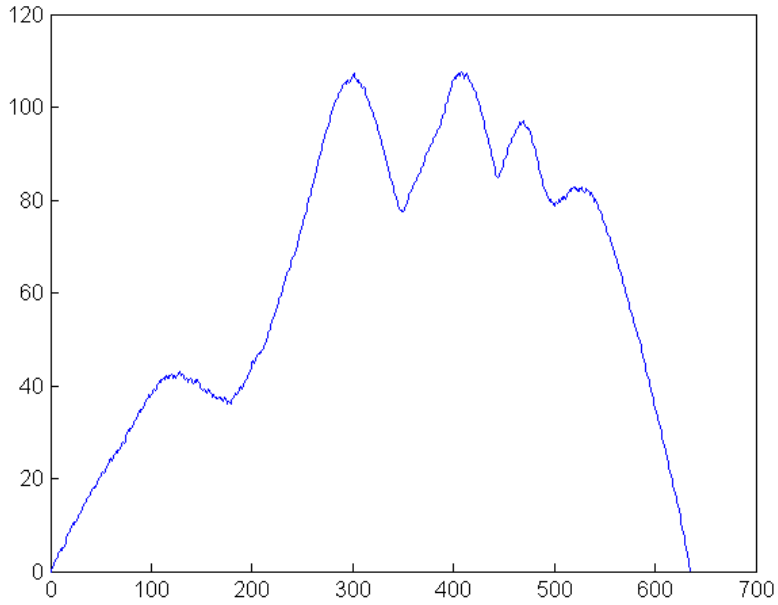

Figure 3.20: “Distance plot” of the facial profile shown in figure 3.16.

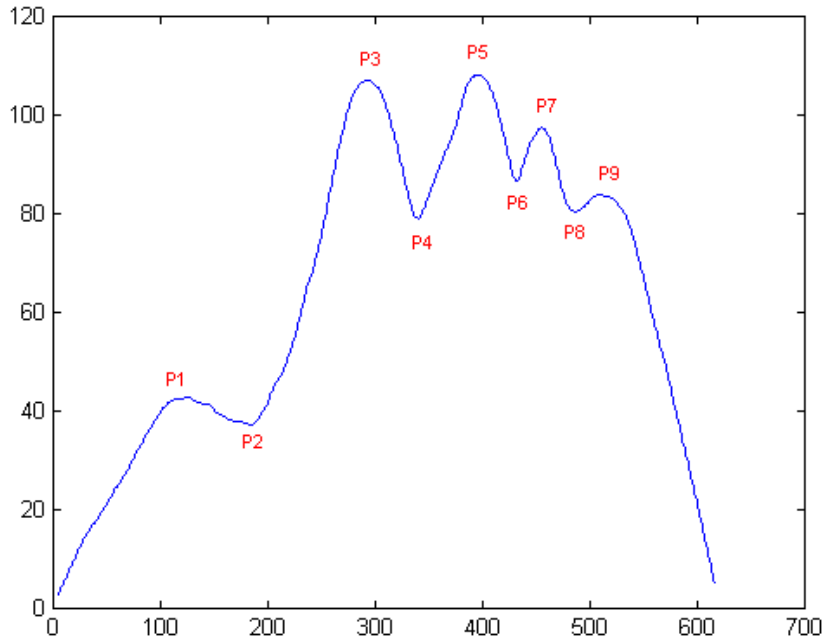

Figure 3.21: The smoothed “distance plot” shown in figure 3.20 ($P1, P2, \cdots, P9$ indicate the initial positions of fiducial points).

With the help of points $P1, P2, \cdots, P9$, the entire facial profile can be divided into nine small curve segments, each of them contains one fiducial point. To locate the exact position of each fiducial, the curvature information corresponding to the small curve segment is used.

3.4.2 Calculation of Curvature

The classical way to compute the local curvature is to consider the intrinsic equations of the curve, $x(l)$ and $y(l)$ versus the arc length l, and to compute the curvature [34]

$$K(l) = \frac{\dot{x}\ddot{y} - \ddot{x}\dot{y}}{\left(\dot{x}^2 + \dot{y}^2\right)^{3/2}} \tag{3.22}$$

where the derivatives are with respect to l.

For a digital curve, the following method is proposed for curvature evaluation. As shown in Figure 3.22, to calculate curvature K_0 at position (x_0, y_0) on a digital curve, m points $(x_{-m}, y_{-m}), (x_{-m+1}, y_{-m+1}), \cdots, (x_{-1}, y_{-1})$ before point (x_0, y_0) and m points $(x_1, y_1), (x_2, y_2), \cdots, (x_m, y_m)$ following point (x_0, y_0) are involved in the following formulas.

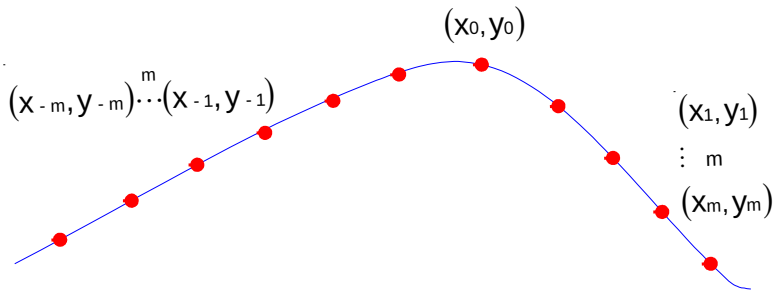

Figure 3.22: Curvature estimation

Defining the digital curve by $y = f(x)$, the curvature K_0 at position (x_0, y_0) is given by

$$K_0 = \frac{d^2y}{dx^2}\left[1+\left(\frac{dy}{dx}\right)^2\right]^{-3/2} \tag{3.23}$$

$$\frac{d^2y}{dx^2} = d_+ - d_-,\ \frac{dy}{dx} = d_{+-},\ \ d_- = \frac{1}{k}\sum_{i=-k+1}^{0}\frac{y_{i-1}-y_i}{x_{i-1}-x_i},\ \ d_+ = \frac{1}{k}\sum_{i=0}^{k-1}\frac{y_i - y_{i+1}}{x_i - x_{i+1}}.$$

Figure 3.23 shows the curvature of each segment determined by points $P1, P2, \cdots, P9$. For instance, to locate the exact position $P3'$ of fidicual point $P3$, the "curvature plot" corresponding to segment $P2P4$ is generated and smoothed by Gaussian smoothing. Fiducial $P3'$ (pronasale), is located at the point with maximum curvature along the "curvature plot".

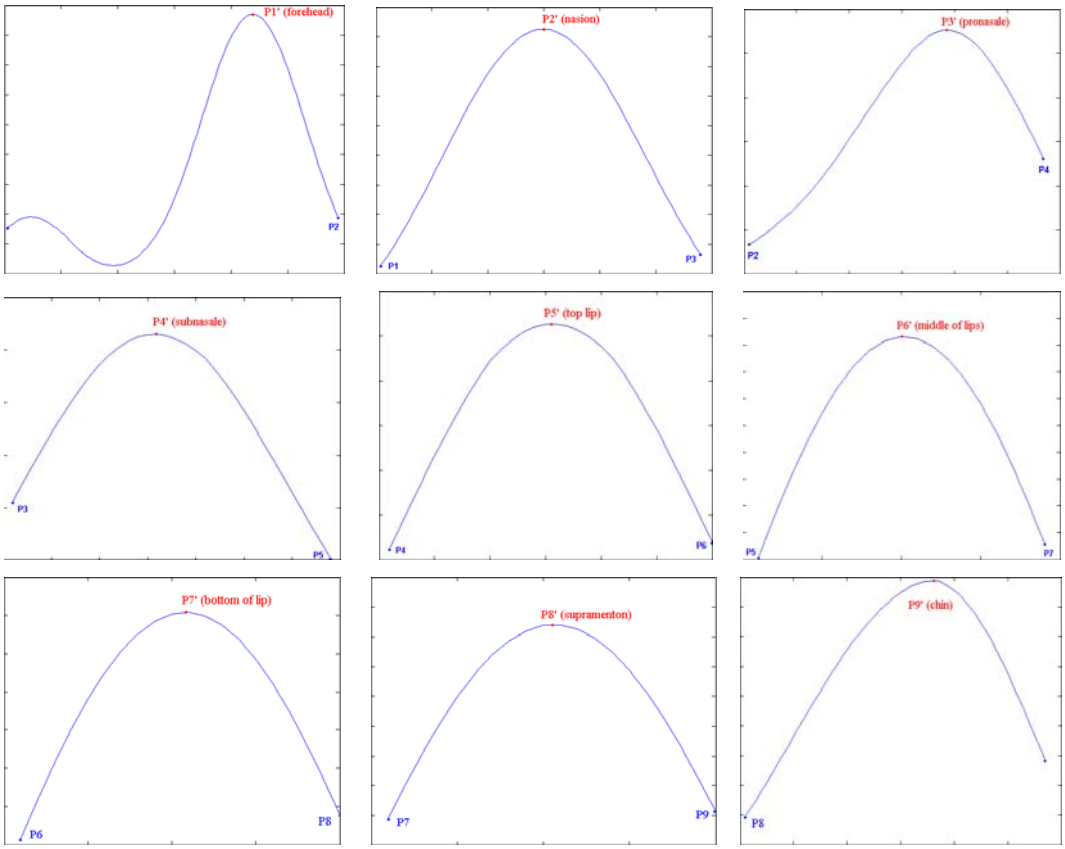

Figure 3.23: The "curvature curves" corresponding to all curve segments divided by $P1, P2, \cdots, P9$. $P1', P2', \cdots, P9'$ indicate the exact fiducials.

3.4.3 Extraction of Fiducial Points

Combining the “distance plot” and “curvature plot”, we can obtain a set of fiducial points for registration between facial profiles. The “distance plot” provides the initial position of each fiducial point, then the exact position is determined by the corresponding “curvature plot”. Figure 3.24 shows the facial profile with nine extracted fiducials: forehead, nasion, pronasale, subnasale, top lip, middle of lips, bottom lip, supramenton, and chin.

Figure 3.24: Facial profile with detected 9 fiducials

3.4.4 Deriving the Geometrical Transformation

Registration is the determination of a geometrical transformation that aligns points in one view of an object with corresponding points in another view of that object or another object. Here, assuming the facial profile ρ_1 extracted from the X-ray image and the facial profile ρ_2 extracted from 3D head are the views to be registered.

At this point, we have a set of matching fiducial pairs. Assuming that this matching set is $\{\mathbf{u}_i, \mathbf{v}_i\}$, $i = 1,2,\cdots,N_c$, where N_c is the total number of correct matching pairs. In general, the 2D point sets $\{\mathbf{u}_i\}$ and $\{\mathbf{v}_i\}$ should satisfy the following equation

$$\mathbf{v}_i = s\mathbf{R}\mathbf{u}_i + \mathbf{T} \qquad for \qquad i = 1,2,\cdots,N_c\,, \tag{3.24}$$

where s is scalar, $\mathbf{R} = \begin{pmatrix} \cos\theta & \sin\theta \\ -\sin\theta & \cos\theta \end{pmatrix}$ represents a rotation matrix, $\mathbf{T} = (t_x, t_y)^t$ is a translation vector, $\mathbf{u}_i = (u_x^i, u_y^i)^t$ is a fiducial point on ρ_1, $\mathbf{v}_i = (v_x^i, v_y^i)^t$ represents a fiducial point on ρ_2, and θ is the orientation difference between ρ_1 and ρ_2.

In order to derive s, $\mathbf{R}$, and $\mathbf{T}$ based on the set of matching fiducial pairs $\{\mathbf{u}_i \Leftrightarrow \mathbf{v}_i\}_{i=1,2,\cdots N_c}$, an error function is introduced as follows:

$$\phi = \sum_{i=1}^{N_c} \left\| s\mathbf{R}\mathbf{u}_i + \mathbf{T} - \mathbf{v} \right\|^2 . \tag{3.25}$$

By minimizing ϕ, a set of optimal solutions can be derived. In [35], Umeyama proposed an effective approach to solve the above problem. From $\partial\phi/\partial\mathbf{T} = 0$, one can obtain

$$\mathbf{T} = \overline{\mathbf{v}} - s\mathbf{R}\overline{\mathbf{u}}\,, \tag{3.26}$$

where $\overline{\mathbf{u}} = \frac{1}{N_c}\sum_{i=1}^{N_c}\mathbf{u}_i$ and $\overline{\mathbf{v}} = \frac{1}{N_c}\sum_{i=1}^{N_c}\mathbf{v}_i$. Substituting Eq. (3.26) into Eq. (3.25) and from $\frac{\partial\phi}{\partial s} = 0$, we have

$$s = \sum_{i=1}^{N_c} \tilde{\mathbf{v}}_i^t \mathbf{R}\tilde{\mathbf{u}}_i \Big/ \sum_{i=1}^{N_c} \tilde{\mathbf{u}}_i^t \tilde{\mathbf{u}}_i\,, \tag{3.27}$$

where $\tilde{\mathbf{u}}_i = \mathbf{u}_i - \overline{\mathbf{u}}$ and $\tilde{\mathbf{v}}_i = \mathbf{v}_i - \overline{\mathbf{v}}$. Substituting Eq.(3.26) and (3.27) into Eq. (3.25) and reorganizing the content of ϕ, we obtain

$$\phi = \sum_{i=1}^{N_c} \tilde{\mathbf{u}}_i^t \tilde{\mathbf{v}}_i - \left[\sum_{i=1}^{N_c} \tilde{\mathbf{v}}_i^t \mathbf{R} \tilde{\mathbf{u}}_i \right]^2 \Bigg/ \sum_{i=1}^{N_c} \tilde{\mathbf{v}}_i^t \tilde{\mathbf{v}}_i \,. \qquad (3.28)$$

Here, minimizing ϕ can be converted into the maximized term

$$\phi' = \left[\sum_{i=1}^{N_c} \tilde{\mathbf{v}}_i^t \mathbf{R} \tilde{\mathbf{u}}_i \right]^2 . \qquad (3.29)$$

Now, the problem at hand is to solve $\mathbf{R}$. We adopt the SVD method to solve $\mathbf{R}$. The procedure is illustrated as follows:

- Calculate the 2×2 matrix $\mathbf{H} = \sum_{i=1}^{N_c} \tilde{\mathbf{u}}_i \tilde{\mathbf{v}}_i^t$.
- Find the SVD of $\mathbf{H}$, i.e., $\mathbf{H} = \mathbf{U} \Lambda \mathbf{V}^t$.
- $\mathbf{R} = \mathbf{V} \mathbf{U}^t$.

3.5 Implementation and Results

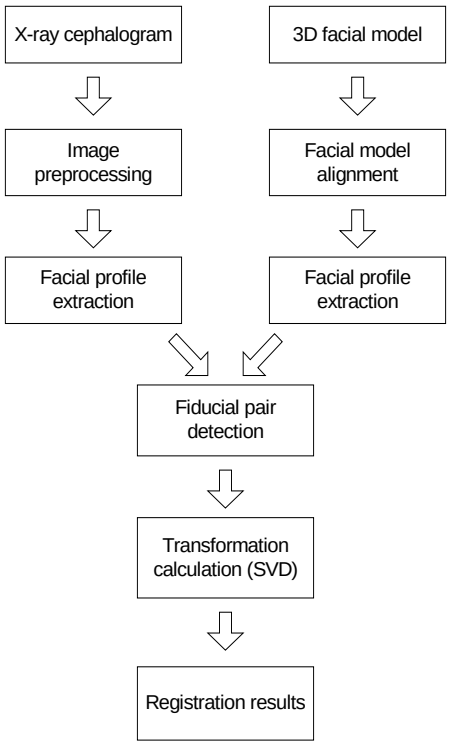

Figure 3.25: Implementation procedure.

The registration procedure may be broken down into three steps for implementation: image preprocessing, facial profile extraction, and geometrical transformation calculation. Figure 3.25 shows the flowchart of this process.

The initial images, lateral cephalogram and 3D facial model, are shown in Figure 3.26.

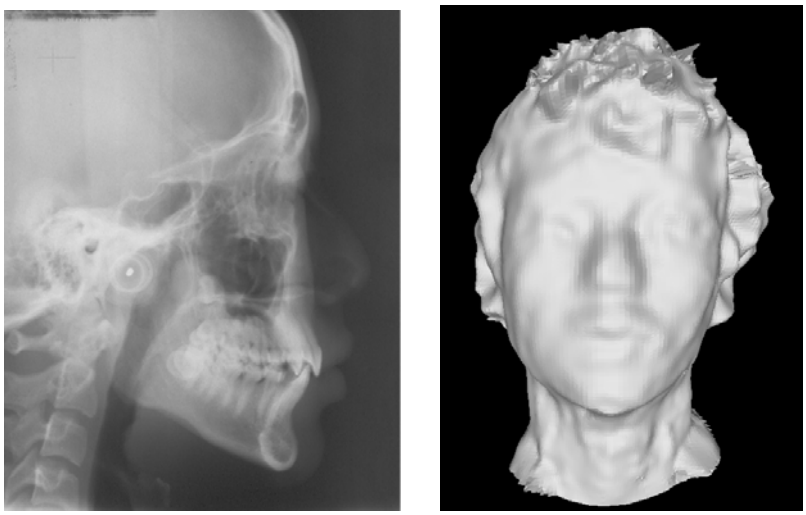

(a) (b)

Figure 3.26: Initial images. (a) Lateral cephalogram. (b) 3D facial model.

The soft tissue information on X-rays is enhanced by applying median filtering, histogram equalization, and logarithm filtering. For the 3D facial model, the numerical parameters for aligning the facial profile to the lateral view are given in Table 3.1. The resultant images are shown in Figure 3.27.

Table 3.1: Transformation for aligning the 3D facial model to the lateral view

Processing procedure	Transformation value
Rotation around *y* axis	88.43°
Rotation around *x* axis	5.10°

* Note: All angles involved in this thesis are consistent with the right hand rule.

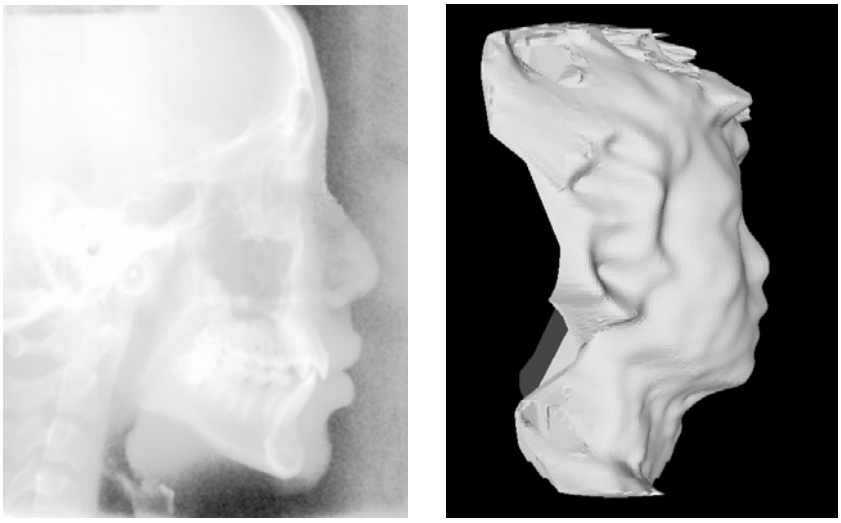

(a) (b)

Figure 3.27: Preprocessed images. (a) Enhanced lateral cephalogram. (b) Aligned facial model.

The facial profiles on both preprocessed images are extracted according to the method we proposed previously. The results are shown in Figure 3.28.

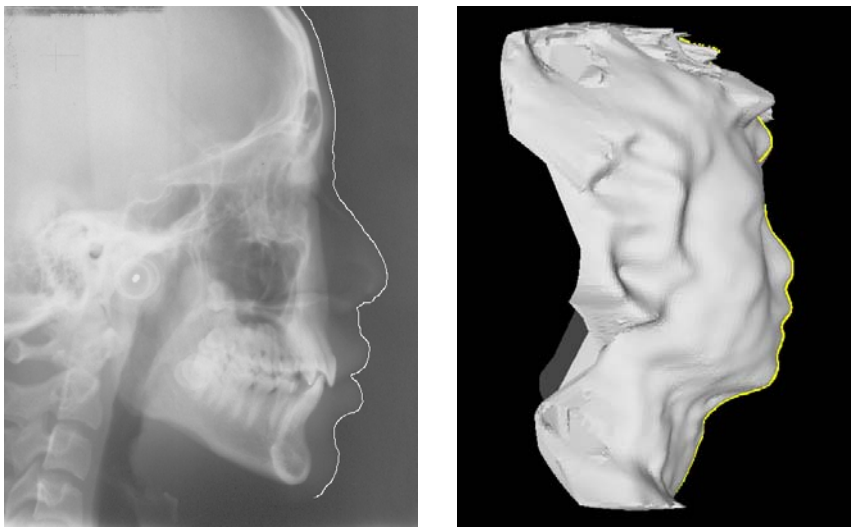

(a) (b)

Figure 3.28: Facial profile extraction. (a) Lateral cephalogram. (b) 3D facial model.

The fiducial pairs are detected from the corresponding facial profiles. The geometrical transformation for the registration is calculated by minimizing the error function. The

relevant parameters applied to the lateral cephalogram are listed in Table 3.2. Finally, we can complete the registration of 3D facial model and 2D lateral cephalogram. The results are shown in Figure 3.29.

Table 3.2: Transformation for the registration of lateral cephalogram and facial model

Transformation	Value
Rotation around *z* axis	-2.27^{o}
Scaling at the *xy* plane	0.56
Translation at the *xy* plane	$[17.04\text{mm} \ -6.80\text{mm}]^{t}$

Figure 3.29: The registration of 3D facial model and lateral cephalogram.

Chapter 4 Dental Cast – Cephalogram Registration

Dental study casts form an essential part of patient records for both diagnostic and medical purposes, and they are often used by the orthodontists for clinical analysis during the course of treatment. However, these casts (Figure 4.1) provide the information only about the crowns of the teeth. Information about the positions and sizes of the roots, which hide within the gums, can only be obtained through conventional methods such as X-rays, CT or MRI. X-rays are cheap, and the radiation exposure of CT and MRI are substantially higher than that received from a lateral cephalogram; therefore the latter is the best choice to register with dental casts in this project.

Figure 4.1: A plaster dental cast model.

In this project, the plaster dental casts are digitized with a surface laser scanner, *Cyberware Rapid 3D Digitizer Model 3030R-HIREZ*, to produce 3D high-resolution images. The data are exported as *VRML* format, and visualized as shown in Figure 4.2.

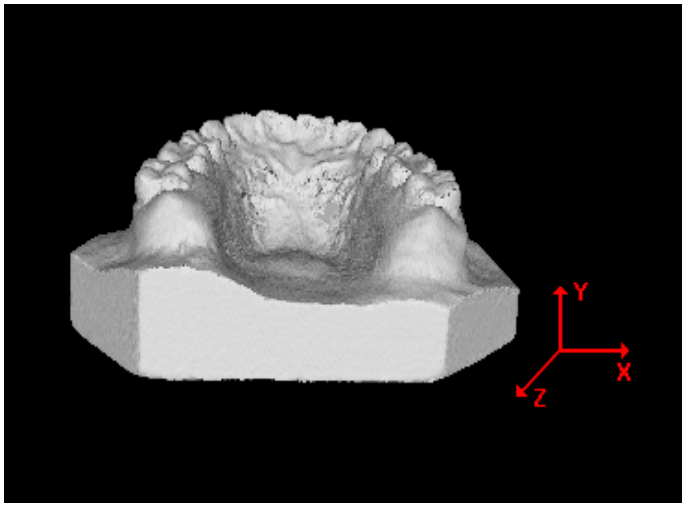

Figure 4.2: The visualization of digitized dental cast.

A set of dental casts for a patient are composed of maxillary and mandibular casts. In general, these casts are digitized by the scanner separately, therefore the alignment of maxillary and mandibular casts is necessary in our project. Such an alignment can be done manually or automatically. Due to the complex mechanism of occlusion, it is not easy to align the upper and lower dental casts accurately in a fully automatic manner.

4.1 Alignment of Maxillary and Mandibular Casts

4.1.1 Rationale

The maxillary and mandibular casts are scanned separately to acquire the detail information about tooth crowns. However, our project aims to register a full dental casts with the corresponding facial model. This requires the maxillary and mandibular casts to be properly aligned with each other. In this section, we present a feasible

method to align the maxillary and mandibular casts (Figure 4.3) automatically with acceptable accuracy.

Figure 4.3: The occluding maxillary and mandibular dentition.

The procedure of the dental casts is as follows: Patients are asked to bite into a container filled with a plaster-like compound and the compound hardens to produce a mould of the teeth. Dental casts are then made from the mould and shaped as shown in Figure 4.1. In addition, the maxillary and mandibular casts are further trimmed simultaneously to get the three flat faces on each cast, marked as F2 (F2'), F3 (F3'), and F4 (F4'), respectively, as shown in Figure 4.4a. This means the corresponding faces on the upper and lower casts should be located in the same plane during the alignment. Furthermore, the largest flat surface of the dental cast is definitely its bottom F1 (F1') as shown in Figure 4.4b. For simplicity, a dental cast can be trimmed to make its back surface (Figure 4.4c) the second largest flat surface with the constraint that the second largest surface should be vertical to the largest one. According to these geometrical information, the upper and lower dental casts can be automatically aligned in x and y directions.

(a)

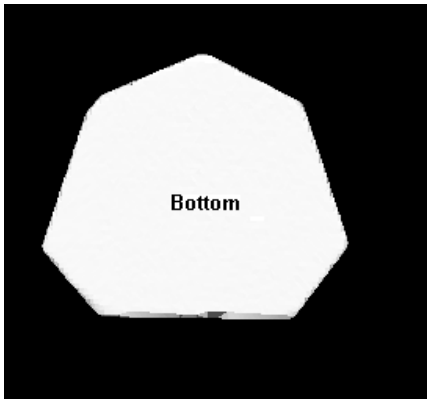

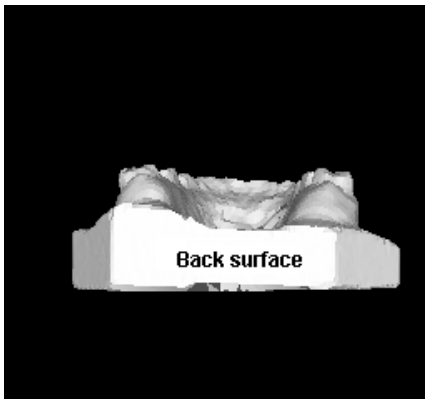

(b) (c)

Figure 4.4: Dental cast: (a)Dental casts with the marked surfaces. (b)The largest surface – Bottom. (c)The second largest surface – Back surface.

4.1.2 Rotation Transformation

4.1.2.1 Detecting the first and second largest faces

After the upper and lower dental casts are digitized separately, they are visualized at the same time. Their initial spatial relationship may be random. Figure 4.5 shows a set of dental casts of the same patient.

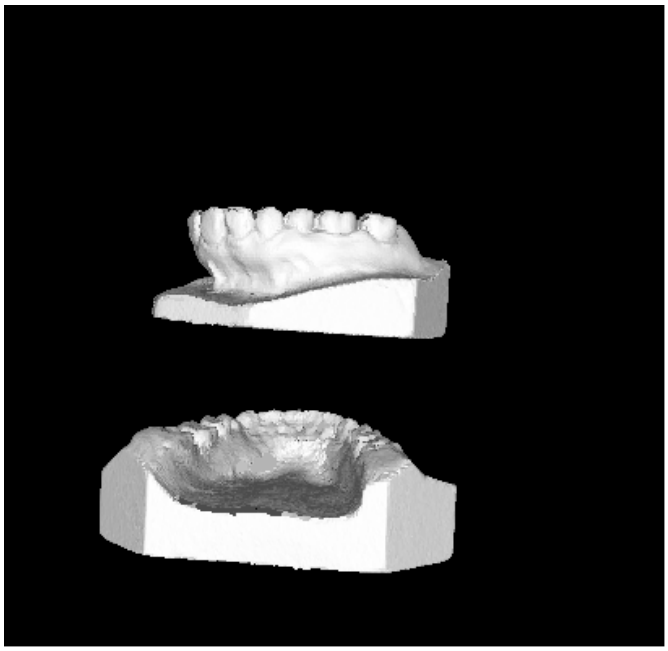

Figure 4.5: Initial spatial of upper and lower dental casts.

The surface of a dental cast is digitized as a triangulated mesh during the scanning, that is, the entire surface is composed of thousands of small triangles. For an object, more triangles means a higher resolution of the scanned surface data. It is obvious that the small triangles should have the same normal if they are in a same plane. Hence, to detect the largest surface on the surface of a dental cast, the normal of each triangle can be used as an indicator. That is to say, the largest surface should contain the greatest number of small triangles with the same normal. Figure 4.6 shows the enlarged triangular mesh and the normal of a triangle abc.

Supposing the coordinates of vertices of triangle *abc* are: $a(x_1, y_1, z_1)$, $b(x_2, y_2, z_2)$, $c(x_3, y_3, z_3)$. Vectors $\mathbf{a}$, $\mathbf{b}$ and $\mathbf{c}$ represent the positions of these three vertices in the 3D space, respectively. Therefore the normal $\mathbf{n}$ of this triangle is calculated using

$$\mathbf{n} = (\mathbf{b} - \mathbf{a}) \times (\mathbf{c} - \mathbf{a}) \qquad (4.1)$$

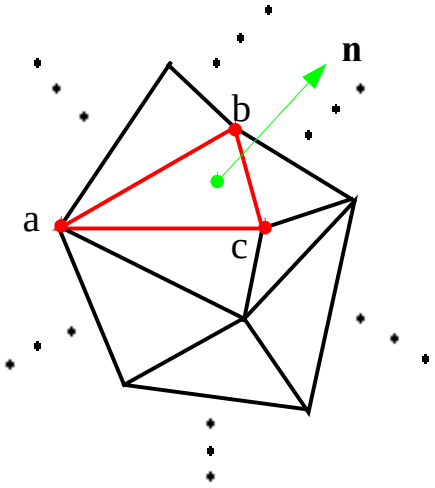

Figure 4.6: Enlarged triangular mesh.

The normals of all triangles are determined and classified within the range of 0º ~ 360° with an interval of 0.25°. The classified normals are sorted according to the corresponding numbers of triangles. The normal with the largest number of triangles should correspond to the normal $\mathbf{n}_1$ of the largest surface, i.e., the bottom of the dental cast in Figure 4.4. For dental cast's back surface, its normal $\mathbf{n}_2$ should be perpendicular to that of the bottom, and corresponds to the second largest number of triangles.

4.1.2.2 Calculation of rotation matrix

From $\mathbf{n}_1$ and $\mathbf{n}_2$, the rotation transformations are calculated. With the corresponding transformation matrix, the bottom is made parallel to the *xz* plane, and the back surface parallel to the *yz* plane. Figure 4.7 shows the results after rotation transformations.

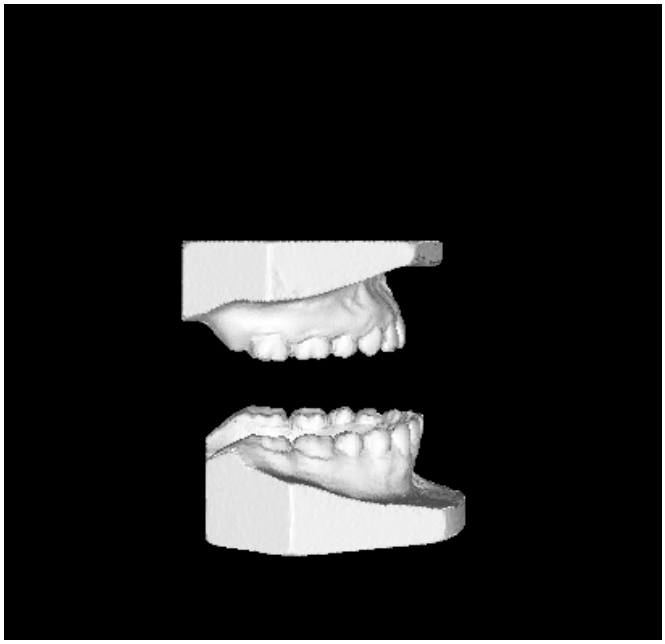

Figure 4.7: Dental casts after rotation transformations.

4.1.3 Translation Transformation

4.1.3.1 Translation along *x* axis

Since the upper and lower dental casts are trimmed simultaneously, it is true that the back surfaces of both casts are located in the same plane and the bottoms are parallel with each other. However, upon the above transformations, although both back surfaces are already made parallel, they are still not in the same plane. The distance between these two surfaces can be calculated. Subsequently, the lower dental cast is translated along the *x* axis by this distance.

4.1.3.2 Translation along *z* axis

Now both back surfaces are in the same plane, but the dental casts may still be staggered, i.e., they are not aligned in the *z* direction. If the midline of the dental cast can be detected, the translation along *z* axis can be calculated by using the upper and

lower midlines. The detailed method to detect the midline of a dental cast is described as follows.

(1) The detection of cusp tips on crowns

Table 4.1 lists all tooth types and the corresponding number of cusp tips on their crowns. As we can see, in general, the number of cusp tips on an adult dental cast is more than 30. Table 4.2 and Figure 4.8 shows the range of values for w_a and w_b in all tooth categories [36]. All measurements were taken using a pair of vernier callipers with precision ±0.02 mm. Here, w_a and w_b are used to measure the size of the incisal or occlusal face of the teeth (Figure 4.8).

Table 4.1 Tooth types and cusp tips on a maxillary/mandibular cast

Tooth Type	Number of the teeth	Number of cusp tips on each tooth
Incisor	4	1
Canine	2	1
Premolar	4	2
Molar	4 ~ 6	4
Total no. of cusp tips on a maxillary/mandibular cast		30-38

Table 4.2: Range of values for l, w_a and w_b in all tooth categories.

Tooth Type	w_a (mm)		w_b (mm)	
	Min.	Max.	Min.	Max.
Incisor	5.60	9.08	5.50	7.54
Canine	5.40	7.66	5.64	7.94
Premolar	6.46	8.26	7.50	11.06
Molar	8.06	11.84	8.64	13.00

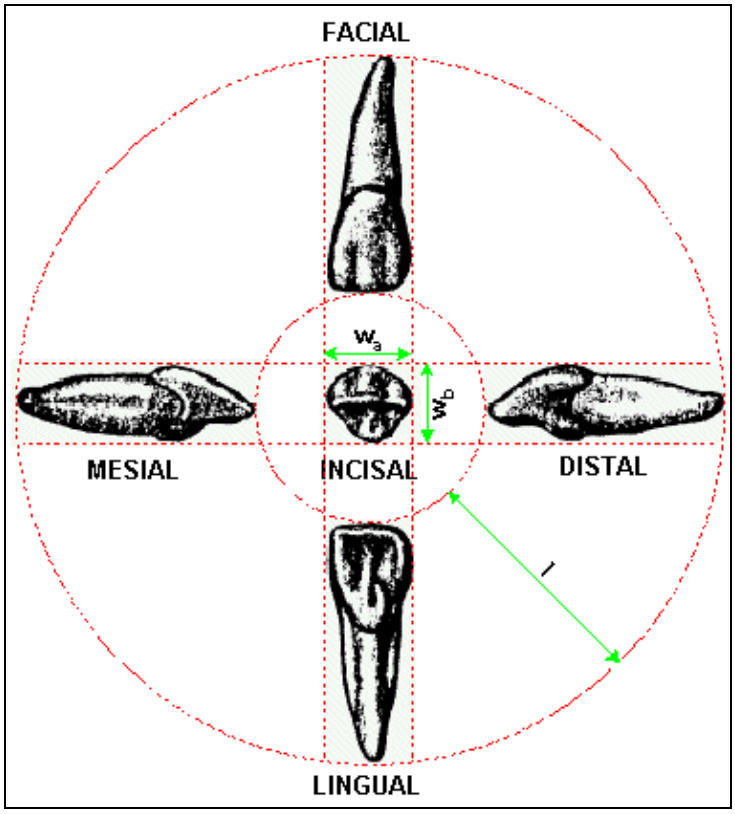

Figure 4.8: Surfaces of incisor.

Using the above information about tooth crowns, cusp tips can be detected on the aligned dental cast upon this point by the following method. The cusp tips on the teeth crowns can be located one by one using local surface minima. The first cusp tip is identified as the lowest vertex on the aligned dental cast. For the second and following cusp tips, they should conform to three constraints: (a) the number of detected cusp tips is less than 30; (b) the cusp tip being identified should be the lowest vertex except for the cusp tips detected already on the dental cast; (c) The distance from this cusp tip to any other detected cusp tip should be larger than 5 mm to guarantee that the cusp tip is located at the local surface minimum. In general, the distance of the neighboring cusp tips is larger than 5 mm, but it is true that this distance constraint may not guarantee all cusp tips on the molars to be detected.

However, the target is to find the dental arch, hence lacking several cusp tips of the molars does not influence the following curve fitting considerably.

Figure 4.9 shows the detected cusp tips (blue points) on the dental cast after the implementation of the above method. In order to have a clear look, the dental cast is rotated and shown in a front view.

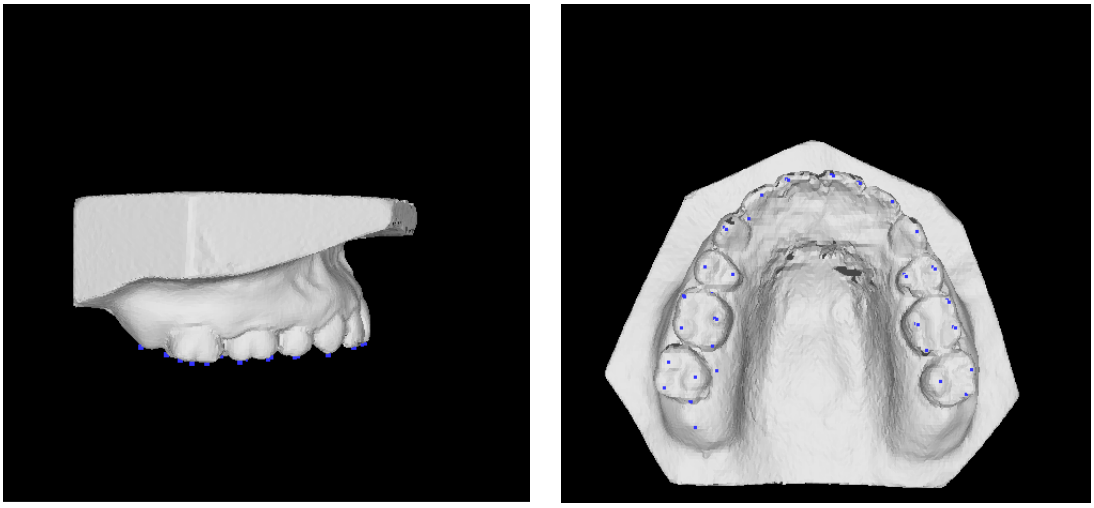

(a) (b)

Figure 4.9 : The extracted cusp tips on a dental cast. (a) Lateral view. (b) Front view.

(2) Remove the inner cusp tips

As shown in Figure 4.10, only the outer cusp tips are used in the regression of dental arch, and the inner cusp tips are removed according to their relative position. The outer cusp tips are sorted and recorded as: $(x_1, y_1, z_1), (x_2, y_2, z_2), \cdots, (x_n, y_n, z_n)$, where n is the number of outer cusp tips.

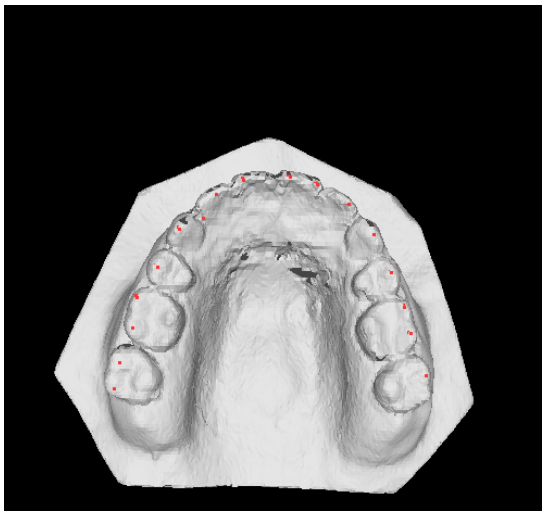

Figure 4.10: Outer cusp tips used by curve fitting.

(3) Regression equation of dental arch

The dental cast has a parabolic shape, so we can use a 2nd degree polynomial $f(x)$,

$$y = a_0 + a_1 x + a_2 x^2 \tag{4.2}$$

to approximate the detected cusp tips, $(x_1, y_1), (x_2, y_2), \cdots, (x_n, y_n)$, where $n \geq 3$, a_0, a_1, a_2 are unknown coefficients. The best fitting curve $f(x)$ should have the minimum least square error. The equation for the least square error is

$$\Pi = \sum_{i=1}^{n} [y_i - f(x_i)]^2 \ . \tag{4.3}$$

To obtain the least square error, the unknown coefficients a_0, a_1, a_2 must yield zero first derivatives:

$$\begin{aligned}
\frac{\partial \Pi}{\partial a_0} &= 2\sum_{i}^{n} \left[y_i - \left(a_0 + a_1 x_i + a_2 x_i^2 \right) \right] = 0 \\
\frac{\partial \Pi}{\partial a_1} &= 2\sum_{i}^{n} x_i \left[y_i - \left(a_0 + a_1 x_i + a_2 x_i^2 \right) \right] = 0 \ . \\
\frac{\partial \Pi}{\partial a_2} &= 2\sum_{i}^{n} x_i^2 \left[y_i - \left(a_0 + a_1 x_i + a_2 x_i^2 \right) \right] = 0
\end{aligned}$$

Expanding the above equations, we have

$$\sum_{i=0}^{n} y_i = a_0 \sum_{i=1}^{n} 1 + a_1 \sum_{i=1}^{n} x_i + a_2 \sum_{i=1}^{n} x_i^2$$
$$\sum_{i=0}^{n} x_i y_i = a_0 \sum_{i=1}^{n} x_i + a_1 \sum_{i=1}^{n} x_i^2 + a_2 \sum_{i=1}^{n} x_i^3 \quad .$$
$$\sum_{i=0}^{n} x^2 y_i = a_0 \sum_{i=1}^{n} x_i^2 + a_1 \sum_{i=1}^{n} x_i^3 + a_2 \sum_{i=1}^{n} x_i^4$$

The unknown coefficients a_0, a_1, a_2 can hence be determined by solving the above linear equations.

In our project, the aim at this step is to find the midline of a dental cast. For simplicity, the equation of the dental arch is estimated by using all the detected outer cusp tips, but the y values of the cusp tips are ignored, i.e., 2D dental arch (on the *xz* plane) is determined by

$$x = a_0 + a_1 z + a_2 z^2 . \qquad (4.4)$$

Hence, the symmetry axis or midline of the dental cast is:

$$z = -\frac{a_1}{2a_2} . \qquad (4.5)$$

Figure 4.11 shows the result, which is a dental arch determined by the least-square 2nd-degree polynomial and its midline on a dental cast.

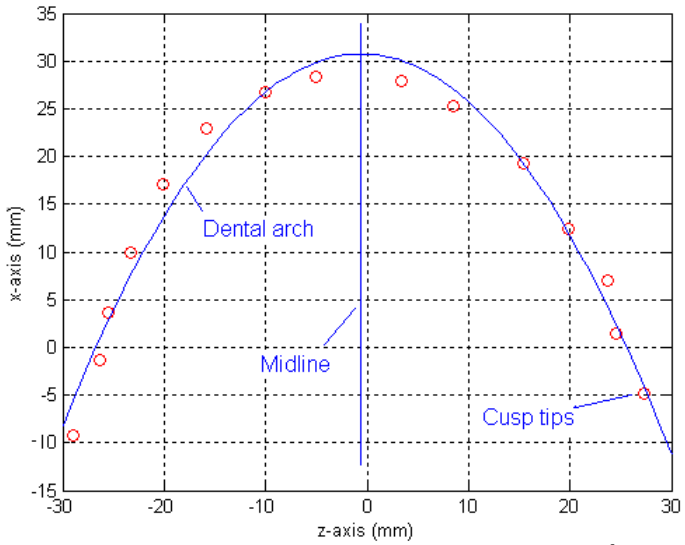

Figure 4.11: The dental arch regression using the least-square 2nd-degree polynomial.

(4) Calculation of the translation distance along *z* axis

After the midlines of upper and lower dental cast are found, the translation along the *z* axis is determined by the distance between them. Figure 4.12 shows the result after performing translations along *x* axis and *z* axis.

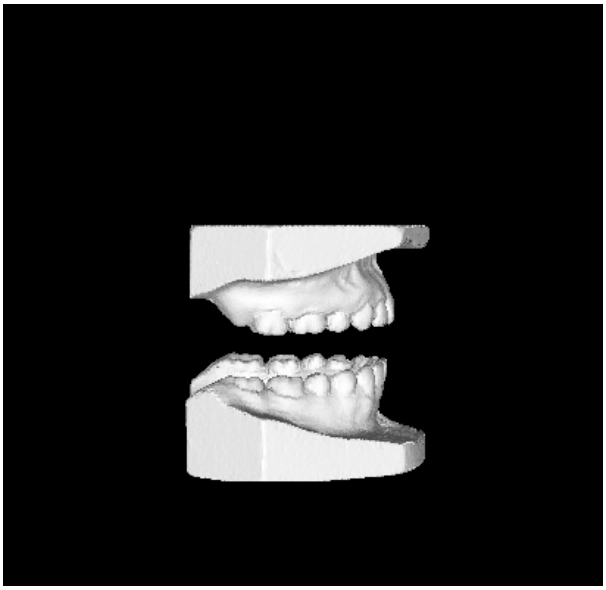

Figure 4.12: Dental casts after translation along *x*, *z* axes.

4.1.3.3 Translation along *y* axis

For the translation along the *y* axis, the vertex with the lowest y coordinate $y_{\min}$ on the upper cast and the vertex with the highest y coordinate $y_{\max}$ on the lower cast are found, so the initial translation distance is $\left|y_{\min} - y_{\max}\right|$. To determine the final translation along $y-axis$, the farthest "face-vertex" distance is found. Here, for any vertex on a cast, its "face-vertex" distance means the shortest one among all distances from itself to each face (i.e., small triangles) on the opposite cast. Then among the "face-vertex" distances of all vertices, the farthest one is selected. The final alignment of the maxillary and mandibular casts is shown in Figure 4.13.

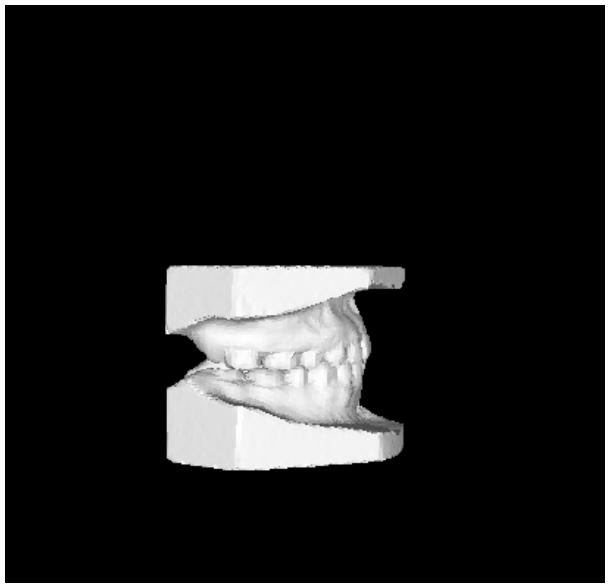

Figure 4.13: Final alignment result of maxillary and mandibular casts.

4.2 Location of Landmarks

During the alignment of maxillary and mandibular casts, the back surfaces of both casts were made perpendicular to the *xy* plane, that is, the dental casts have been transformed to the same lateral view as the cephalogram. Hence, the remaining task is to rotate and translate the full dental casts to the correct position on the cephalogram.

Since the useful information on dental casts only exist in the crowns, the full dental casts are trimmed automatically to remove the unrelated parts before registration. Here, two planes parallel to the *xz* plane are used to cut off the upper third and lower third part of the full dental casts. The tooth crowns are kept as shown in Figure 4.14.

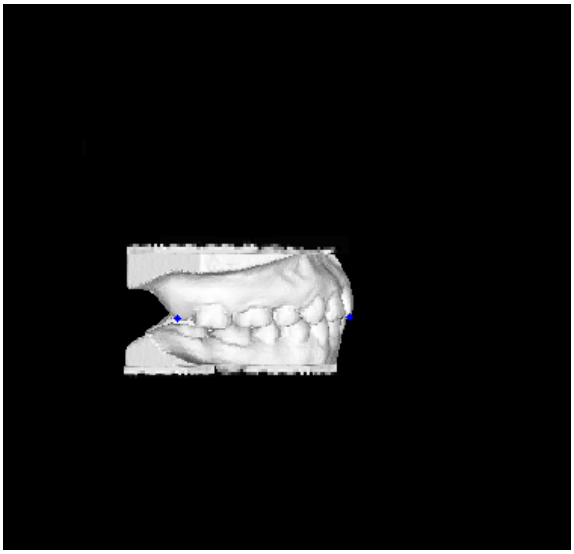

Figure 4.14: Trimmed dental casts with the landmarks: the superior incisor and the last upper molar.

To register the dental casts and the lateral cephalogram, two landmarks, the superior incisor and the last upper molar, are located manually on both images. Supposing the two landmarks in cephalogram are $u_1(x, y)$ and $u_2(x, y)$, while the corresponding landmarks on dental cast are $v_1(x, y)$ and $v_2(x, y)$, then the 2D geometric transformation is calculated by minimizing the least mean square error between these two pairs of landmarks.

4.3 Implementation of Registration

We applied the methods described in section 4.1 and 4.2 on a set of data collected from the same patient. The transformation parameters used during the alignment of maxillary and mandibular casts are listed in Table 4.3. And the geometric

transformation for the registration of dental casts with lateral cephalogram is given in Table 4.4. Finally, the entire process and the results obtained are shown in figure 4.15.

Table 4.3: Transformation parameters for the alignment of maxillary and mandibular casts

Alignment procedure	Transformation value		Effect of transformation	
	Maxillary	Mandibular	Maxillary	Mandibular
Rotation around *x* axis	-1.00°	1.25°	Bottom towards up (+*y*)	Bottom towards down (-*y*)
Rotation around *z* axis	175.50°	-3.00°		
Rotation around *y* axis	57.25°	43.25°	Back surface towards left (-*x*)	Back surface towards left (-*x*)
Translation along *x* axis	0 mm	1.05 mm	Two back surfaces are aligned	
Translation along *z* axis	0 mm	0.30 mm	The midlines of dental casts are aligned	
Translation along Y axis	0 mm	21.17 mm	The dental casts are aligned along *y* axis	

Table 4.4: Transformation parameters for the registration of dental casts with lateral cephalogram

Rotation around *z* axis	Scaling	Translation (in the *xy* plane)
Angle = -12.29° Matrix = $\begin{bmatrix} 0.9771 & -0.2126 \\ 0.2126 & 0.9771 \end{bmatrix}$	0.87	$\begin{bmatrix} 19.14 \\ -41.69 \end{bmatrix}$

Note: The position of the lateral cephalogram has been determined after the registration with facial model. The transformation given in Table 4.4 is applied to the aligned full dental cast.

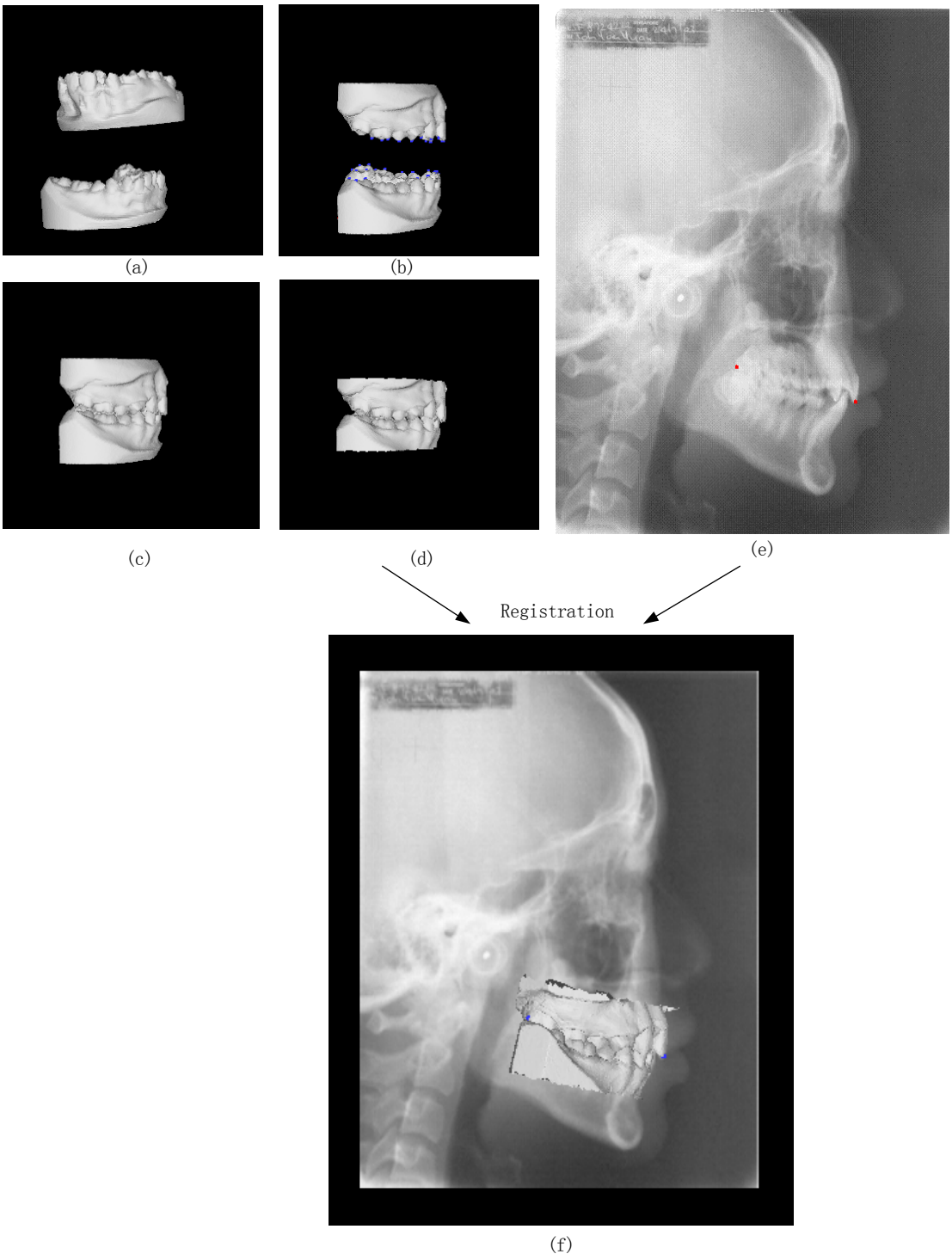

Figure 4.15: The entire process of registration between dental casts and cephalogram. Dental casts: (a) Initial position; (b) After rotation; (c) After translation; (d) Trimmed casts with landmarks. (e) X-ray with landmarks. (f) The registration result of dental casts with X-ray

4.4 Integration of Facial Model and Dental Casts

The registration of the facial model with lateral cephalogram has been described in detail in Chapter 3. This chapter has focused on the registration between the lateral cephalogram and dental casts. With the lateral cephalogram as the reference object, the spatial relationship between the facial model and dental casts can be determined consequently. At first, the lateral cephalogram is superimposed on 3D facial model. Then the 3D dental cast is registered with the above X-ray, and at the same time, the data of the dental cast and facial model are integrated together. Figure 4.16 shows the final registration result.

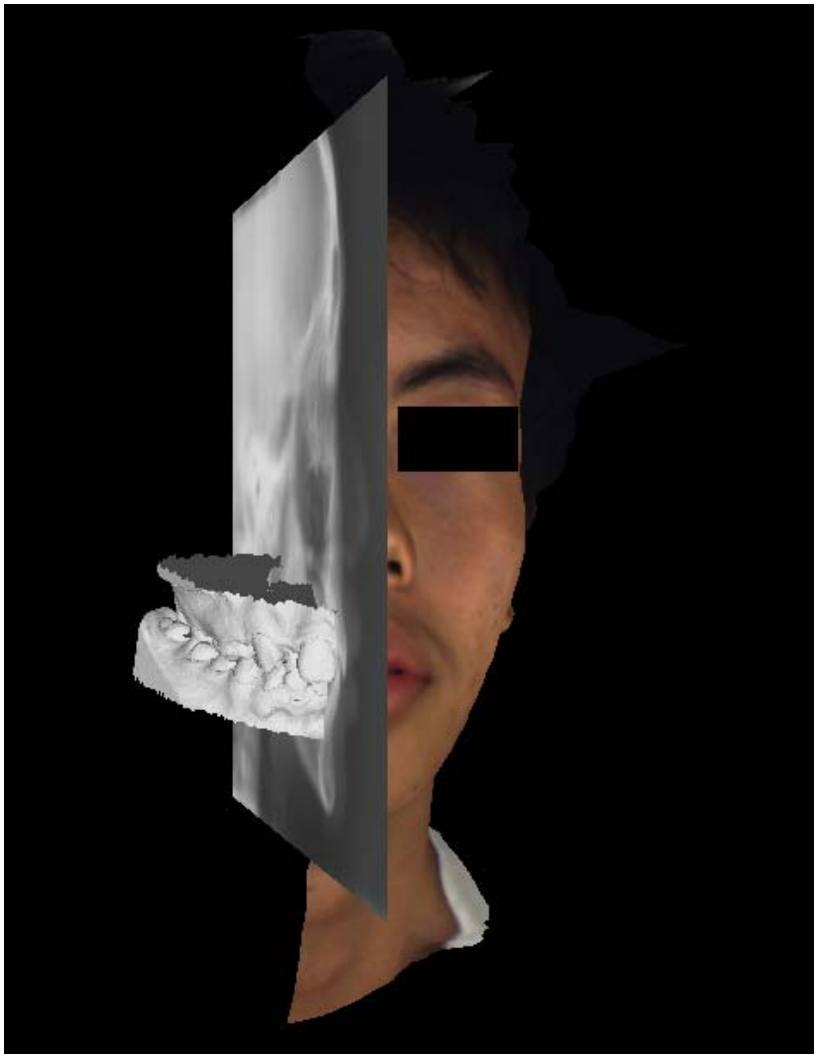

Figure 4.16: Registration result of dental cast and facial model.

Chapter 5 Experimental Results and Discussion

With the algorithms presented in Chapters 3 and 4, the final multimodal dentofacial registration system is built. This Chapter aims to collect more data to test the performance of the system. At first, the important intermediate steps involved in the entire project, namely, facial profile extraction, facial profile-based registration, alignment of upper and lower dental casts are examined. Then another full set of data was acquired from the same patient to test the entire performance of the registration system. This set of data similarly includes dental casts, lateral cephalogram and facial model.

5.1 Experimental Setup

5.1.1 Dental Casts

To obtain the 3D surface data of the teeth, the dental casts are digitized using a laser scanner, *Cyberware Rapid 3D Digitizer Model 3030R-HIREZ* (Figure 5.1), to produce 3D high-resolution images. During the scanning operation, the scanner shines a low-intensity laser stripe on the object to create a lighted profile, and an image sensor captures this profile from two viewpoints. The geometry of the profile is subsequently calculated by simple triangulation. Surface depth information is obtained with a resolution better than 0.2 mm and scanning motions are controlled by software-driven servomotors. The specifications of the scanner are shown in Table 5.1 [37].

Figure 5.1: Cyberware scanner [37].

Table 5.1: Specifications of the laser scanner

Spatial resolution	*X*	Depends on motion platform speed; 30 samples per second in x; typically 500µm to 2mm
	Y	313µm
	Z	50 to 200µm depending on surface quality

5.1.2 Lateral Cephalogram

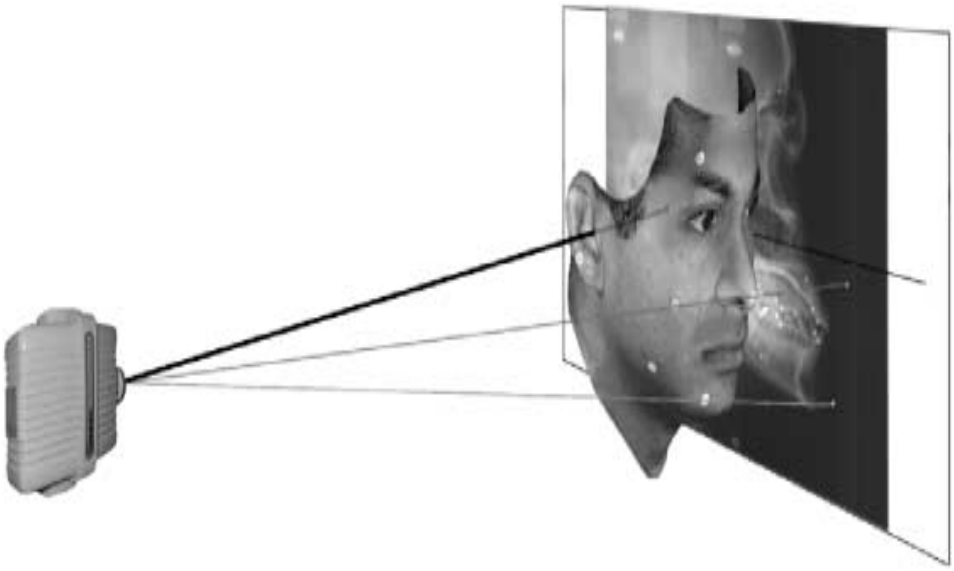

Figure 5.2: The symbolic geometry of 2D projection cephalogram [3].

For the lateral cephalogram, it was taken by a computed radiograph unit and printed on acetate film. Figure 5.2 symbolically illustrates the process: x-rays from a point source pass through the subject and register on a radio-sensitive film or other receiver located beyond the subject. The shadows of objects on or in the subject's skull are represented on the film surface at gray scale inversely proportional to the density of the object. In our project, no further details about the underlying image geometry were known, therefore we assume that it was obtained by a parallel projection. Subsequently, the lateral cephalograms which were approximately the size of A4 paper were scanned to a digital format using *Agfa's ARCUS II* Scanner and *Fotolook* 2.08β *Standalone Software* running under *Windows* NT. The obtained images have a resolution of 75dpi and 8 bits per grey value.

5.1.3 3D Facial Model

Figure 5.3: FaceVision 600 Series (Geometrix Inc., Appendix B).

For the 3D facial model, it is scanned and digitized by a face capture system called *FaceVision* (Figure 5.3). *FaceVision* 600 series is a 3D biometric enrollment station that includes six high-speed, high-resolution cameras mounted in a rigid frame containing a complete optimized lighting system. The cameras are arranged in three pairs, each of which acquires a 3D patch from one view of the subject's face (front, right, and left). The three patches are automatically merged together into a precise ear-to-ear 3D facial model, including compression into a 3D facial shape analysis template for rapid identity comparisons [38]. The acquired data can be exported into the following formats: Viewpoint Metastream, 3D Studio, Alias Wavefront, Autodesk DXF, and W3C VRML.

5.2 Facial Profile Extraction

5.2.1 Lateral Cephalogram

5.2.1.1 Experiment goals

The motive of this experiment is to test the performance of facial profile extraction technique on lateral cephalograms. 16 patients' lateral cephalograms are collected and digitized by *Agfa's ARCUS II* scanner. The method proposed in Chapter 3 is applied to each cephalogram image to extract the patient's facial profile.

5.2.1.2 Results and discussion

All the results are shown in Figure 5.4. The extracted facial profiles are superimposed onto the original cephalograms in order to check whether the soft tissue profiles are extracted correctly.

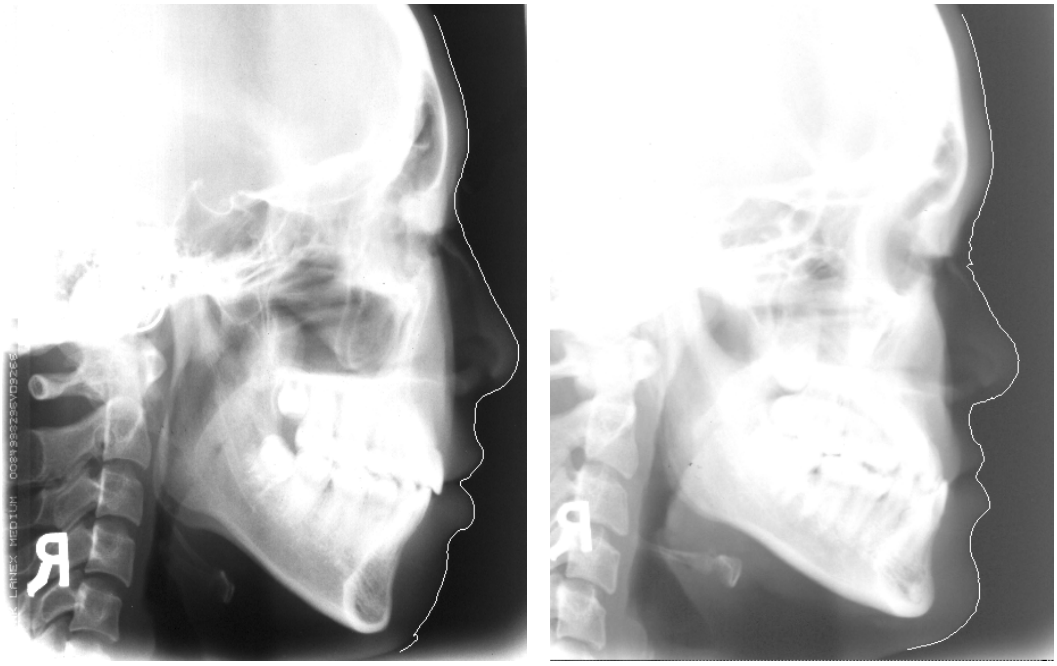

(1) (2)

(3)

(4)

(5)

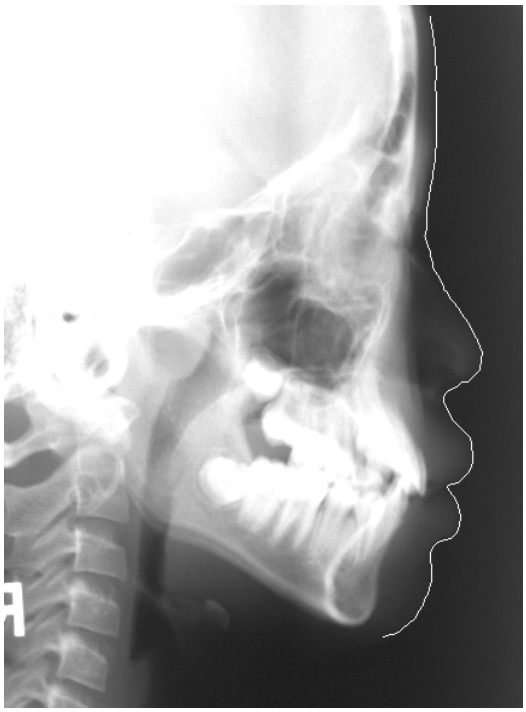

(6)

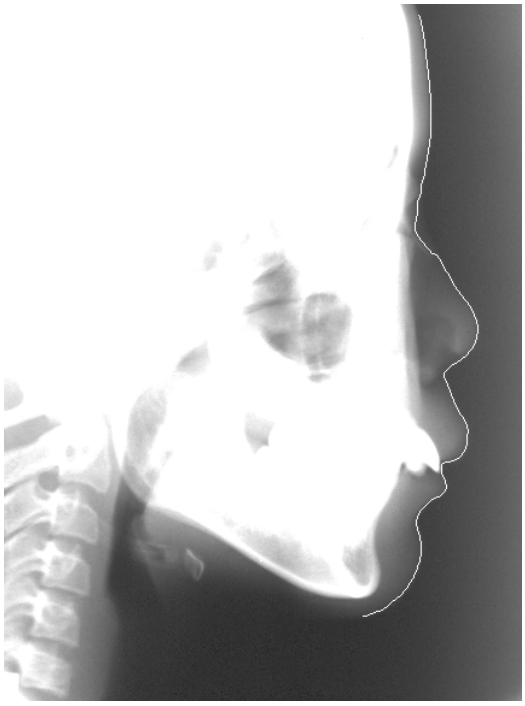

(7)

(8)

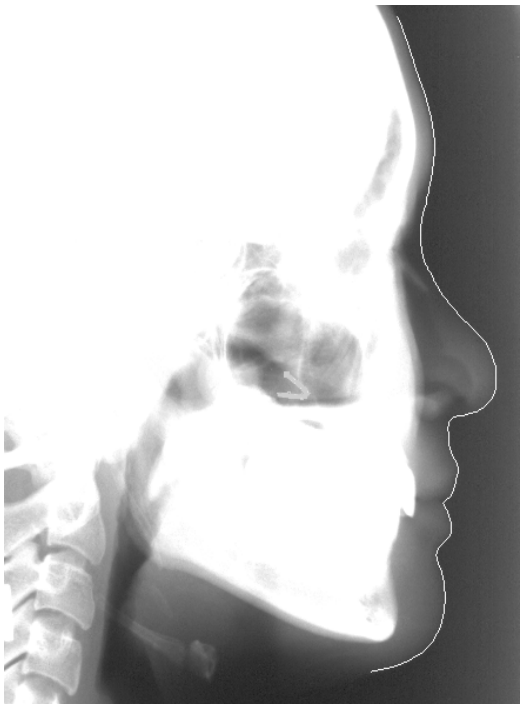

(9)

(10)

(11)

(12)

(13)

(14)

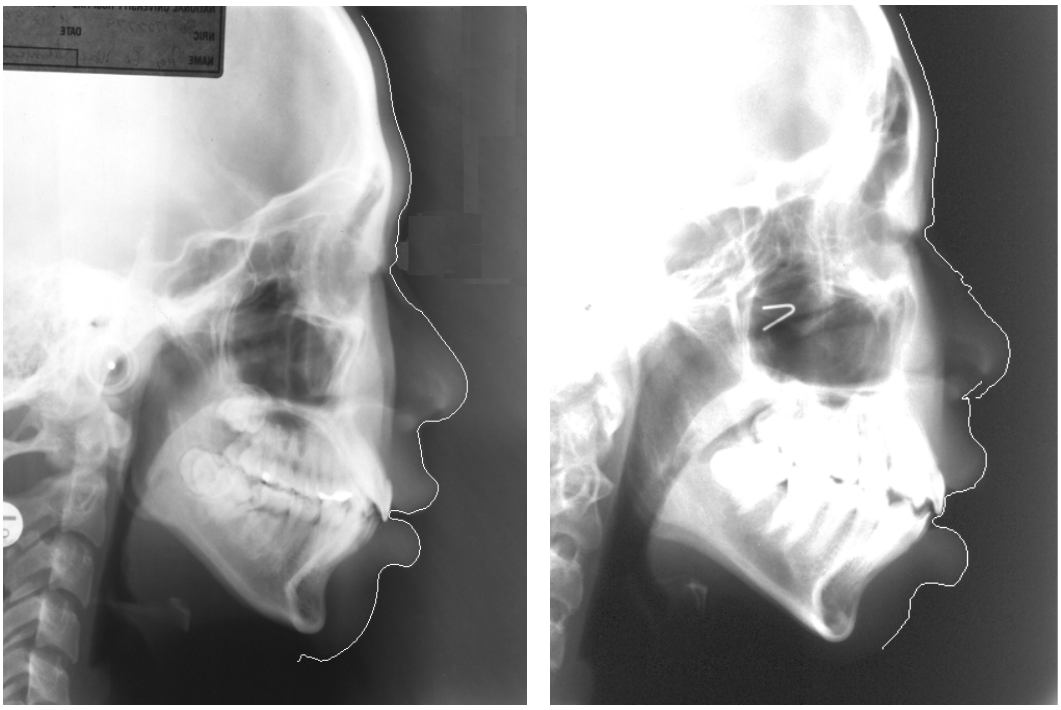

(15) (16)

Figure 5.4: 16 patients' cephalograms with extracted facial profiles.

As we can see, most of the images show good results, that is to say the edge detection method proposed in this thesis is successful in the facial profile extraction on X-ray images. Nearly all the extracted facial profiles trace correctly the contour of the facial soft tissue, except that the edges extracted near the nasion are not accurate enough in some images. Referring to image (4) and image (16), we see that those edges go further inside than their actual positions. This is because the soft tissue around the nasion is difficult to identify in the X-ray. As shown in Figure 5.5, even after the soft tissue in enhanced by histogram equalization and logarithm filtering, the edge near the nasion (marked as red segment) cannot be detected successfully. The edge detected (marked as white segment) is actually located at the nasal cartilage.

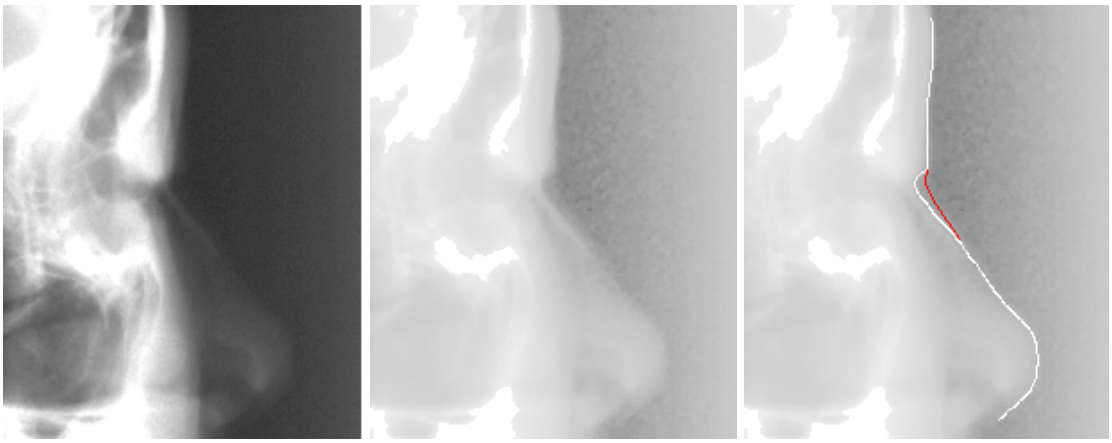

(a) (b) (c)

Figure 5.5: The edge detection near the nasion. (a) The original X-ray. (b) Enhanced soft tissue. (c) Edge detection.

Furthermore, there exist small gaps in the extracted facial profiles of image (14) and (16). Upon further observation, we see that the areas where the gaps are located are quite dark and the edges are submerged in the background. Hence the edge detector fails to detect the correct edges that make up of the facial profile, but instead the stronger edges beside the facial profile are detected.

5.2.2 3D Facial Model

5.2.2.1 Experimental goals

In order to extract the 2D facial profile from a 3D facial model, Chapter 3 presents an approach based on detecting the ridge of the nose. This experiment is designed to investigate its validity. Five subjects were collected and each of them was taken a scan using *FaceVision* scanner.

5.2.2.2 Results and discussion

The facial profile extraction technique presented in Chapter 3 has been applied to five models. The results for all images can be seen in Figure 5.6. Column (a) contains the front views of the 3D facial models aligned using the nose-ridge detection technique. The straight lines indicate the planes passing through the nose bridge, and the green points are the detected nose-ridge points. Column (b) contains the facial models with the extracted facial profiles.

As shown in Figure 5.6, this facial profile extraction performs well since the extracted facial profiles approximately separate the head into symmetrical left and right halves. However, as discussed in Chapter 3, the constraint is that a head should be nearly upright or tilted slightly ($< 5^{\circ}$). Otherwise, the nose ridge points cannot be detected correctly, which would affect the transformation for the alignment of the head.

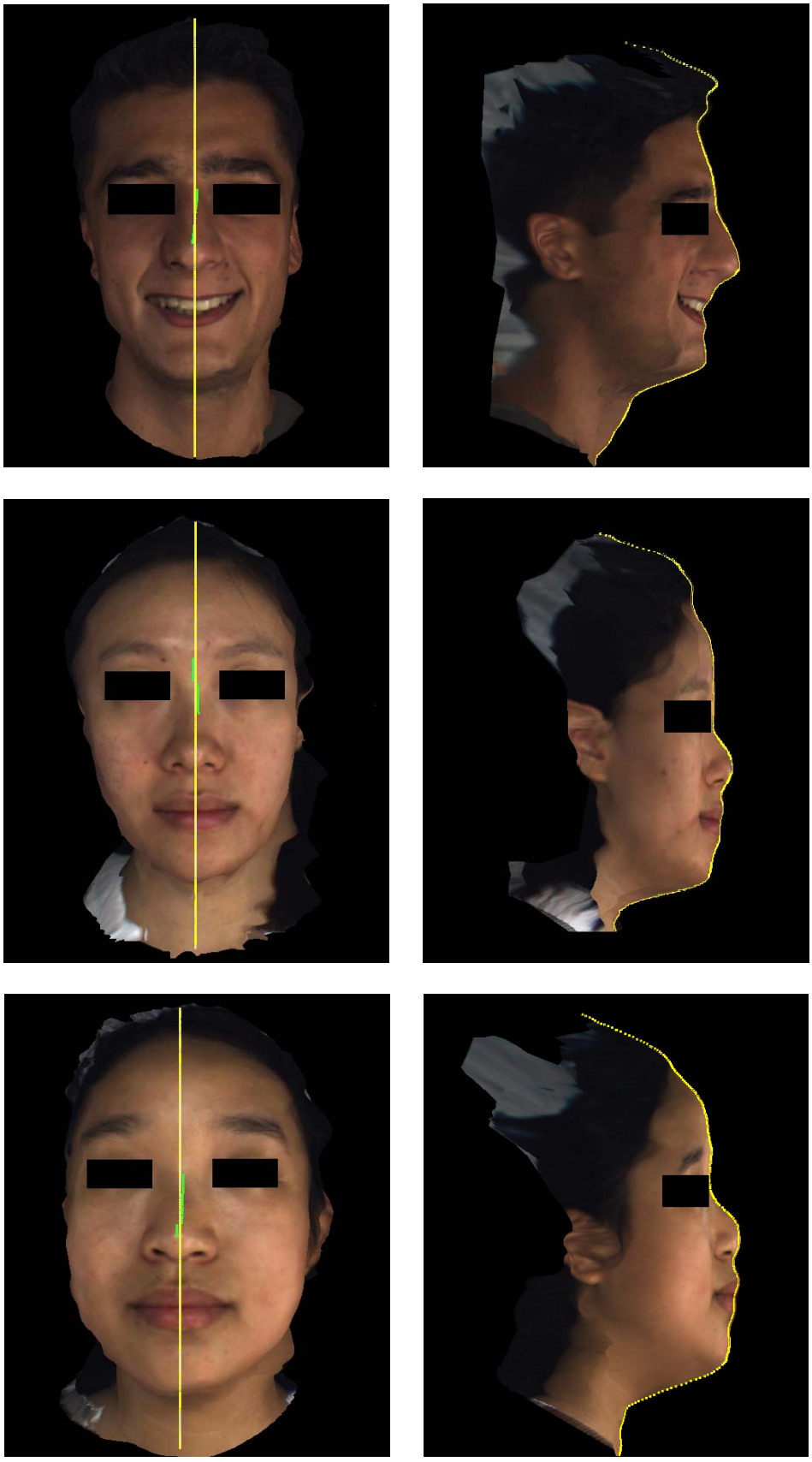

(a) (b)

(a) (b)

Figure 5.6: Facial models. Column (a) contains the subjects' frontal view with detected nose-ridge points and the planes used to extract the profiles. Column (b) contains the extracted profiles.

5.3 Registration Between Facial Profiles

As described in Chapter 3, to register the 3D facial model and 2D lateral cephalogram, the corresponding 2D facial profiles should be extracted first, then fiducial points along the profiles are detected based on the curvature information. Finally, the geometrical transformation is determined from all fiduicial points by minimizing error function. In order to test the accuracy of registration between facial profiles, the following experiments are designed.

5.3.1 Rigid Transformation

In this experiment, only the translation and rotation are involved. Supposing we have a lateral cephalogram I, another lateral cephalogram I' is obtained by doing some translation and rotation (transformation T_1) to I. Then the corresponding facial profiles are extracted and analyzed. Fiducial points along facial profiles are used to determine the image transformation T_1'. The accuracy of the registration result can be indicated by comparing the calculated geometrical transformation T_1' with T_1.

Figure 5.7 shows the image I and image I'. The applied geometrical transformation T_1 between I and I' is:

$$\begin{aligned} I' &= \mathbf{R}I + \mathbf{T} \\ &= \begin{bmatrix} \cos 10^\circ & \sin 10^\circ \\ -\sin 10^\circ & \cos 10^\circ \end{bmatrix} \times I + \begin{bmatrix} 100 \\ 15 \end{bmatrix}. \end{aligned}$$

The extracted facial profiles and fiducial points along them are also shown in figure 5.7. As for the registration result, it is shown in figure 5.8.

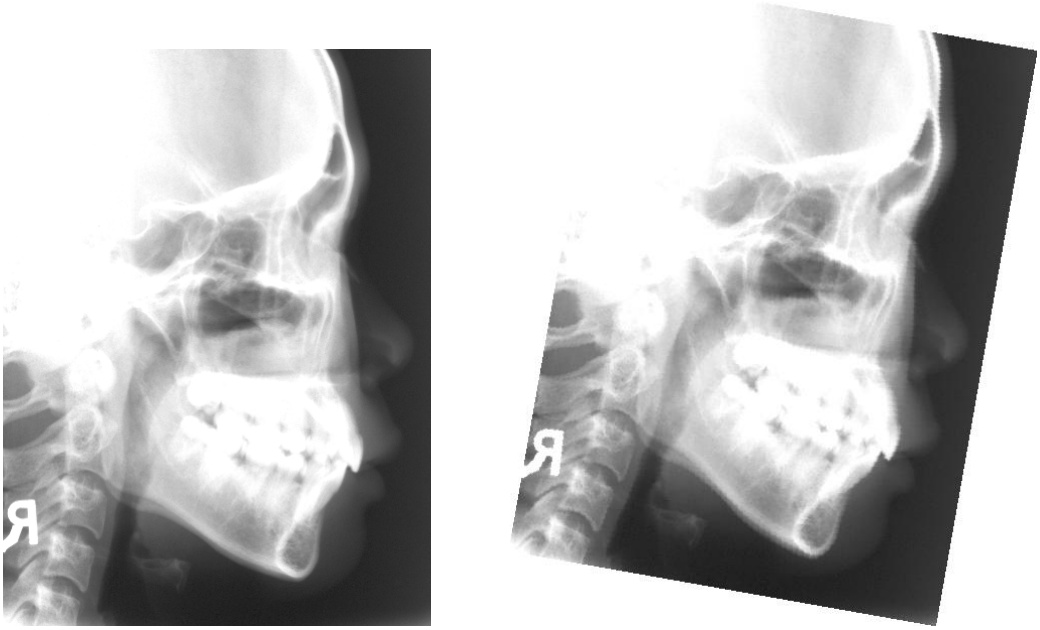

(a) (b)

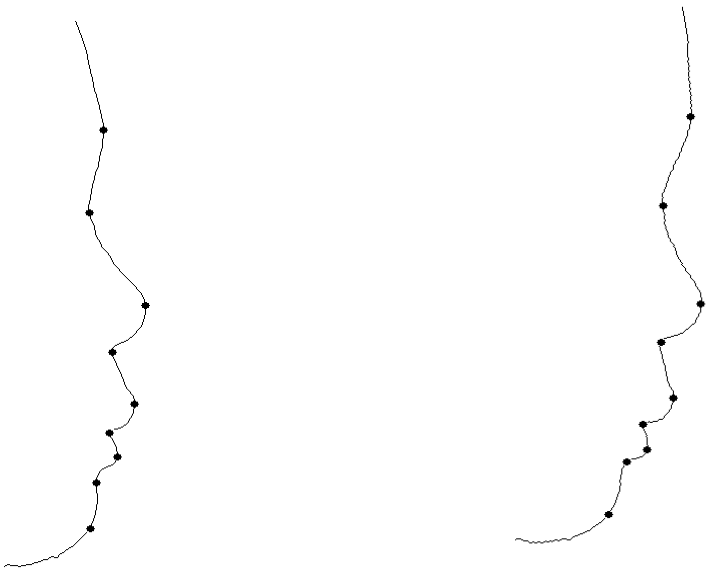

(c) (d)

Figure5.7: (a) Cephalogram image I . (b) Cephalogram image I'. (c) Facial profile with fiducial points extracted from image I . (d) Facial profile with fiducial points extracted from image I'.

Figure5.8: The registration result of the two facial profiles.
(green: image I'; red: image I; blue: the common part of the two images)

The calculated geometrical transformation between images I and I' is:

$$I' = \begin{bmatrix} \cos 9.956^\circ & \sin 9.956^\circ \\ -\sin 9.956^\circ & \cos 9.956^\circ \end{bmatrix} I + \begin{bmatrix} 98 \\ 16 \end{bmatrix}.$$

Table 5.2: The accuracy of the registration of facial profiles.

Transformation	Rotation (°)	Translation (pixel)
T_1	10°	(100,15)
T_1'	9.956°	(98, 16)
Difference (T_1' -T_1)	-0.044°	(-2,1)

Comparing geometrical transformation T_1' with T_1, the result is shown in Table 5.2. The difference between T_1' and T_1 is quite small; the difference between the rotation angles is only 0.004° and the translation error is within 1 or 2 pixels. That means the registration method proposed is feasible and its accuracy is satisfactory.

5.3.2 Non-rigid Transformation

The procedure of this experiment is similar to the experiment above except that the scaling factor is involved in transformation. Supposed we still have cephalogram image I, image I'' is obtained by non-rigid transforming image I using T_2:

$$\begin{aligned} I' &= s\mathbf{R}I + \mathbf{T} \\ &= 1.5 \times \begin{bmatrix} \cos 20^{\circ} & \sin 20^{\circ} \\ -\sin 20^{\circ} & \cos 20^{\circ} \end{bmatrix} \times I + \begin{bmatrix} 45 \\ 165 \end{bmatrix}. \end{aligned}$$

Using the same method, we calculated the geometrical transformation T_2', and the comparison between T_2 and T_2' is shown in Table 5.3. Finally, the registration result is shown in Figure 5.9.

Table 5.3: The accuracy of the registration of facial profiles

Transformation	Rotation (°)	Scaling	Translation (pixel)
T_2	20°	1.5	(45,165)
T_2'	19.950°	1.494	(46, 165)
Difference ($T_2' - T_2$)	-0.050°	0.006	(1,0)

Figure5.9: The registration result of the two facial profiles.
(green: image I''; red: image I; blue: the common part)

5.3.3 Discussion

Figure 5.8 and 5.9 show the results of the registration of facial profiles with different pose and size. The two facial profiles to be registered are colored as red and green separately, with the red one as a reference target. After registration, the common part is colored as blue. Observing the registration results, we can find that the facial profiles are well registered, since the green facial profile approaches the red reference target closely.

For measuring the quantitative accuracy, we compare the corresponding geometric transformation $T\ (T_1, T_2)$ with $T'\ (T_1', T_2')$, T is the pre-known geometric transformation and T' is the calculated one by our proposed registration method. From Table 2 and Table 3, T' is slightly different from T; the rotation angle difference is as small as 0.05º, and the discrepancy of translation is within 2 pixels. Generally, the desired registration accuracy should be within an error range of ± 1 mm and $\pm 1^{\circ}$, therefore, our registration accuracy meet the medical requirement.

5.4 Maxillary and Mandibular Casts Alignment

5.4.1 Experimental Goals

The maxillary and mandibular dental casts can be aligned properly according to their geometrical relationship. We now test the performance of the alignment method

described in Chapter 4 using three pairs of dental casts. Figure 5.10 shows the alignment results.

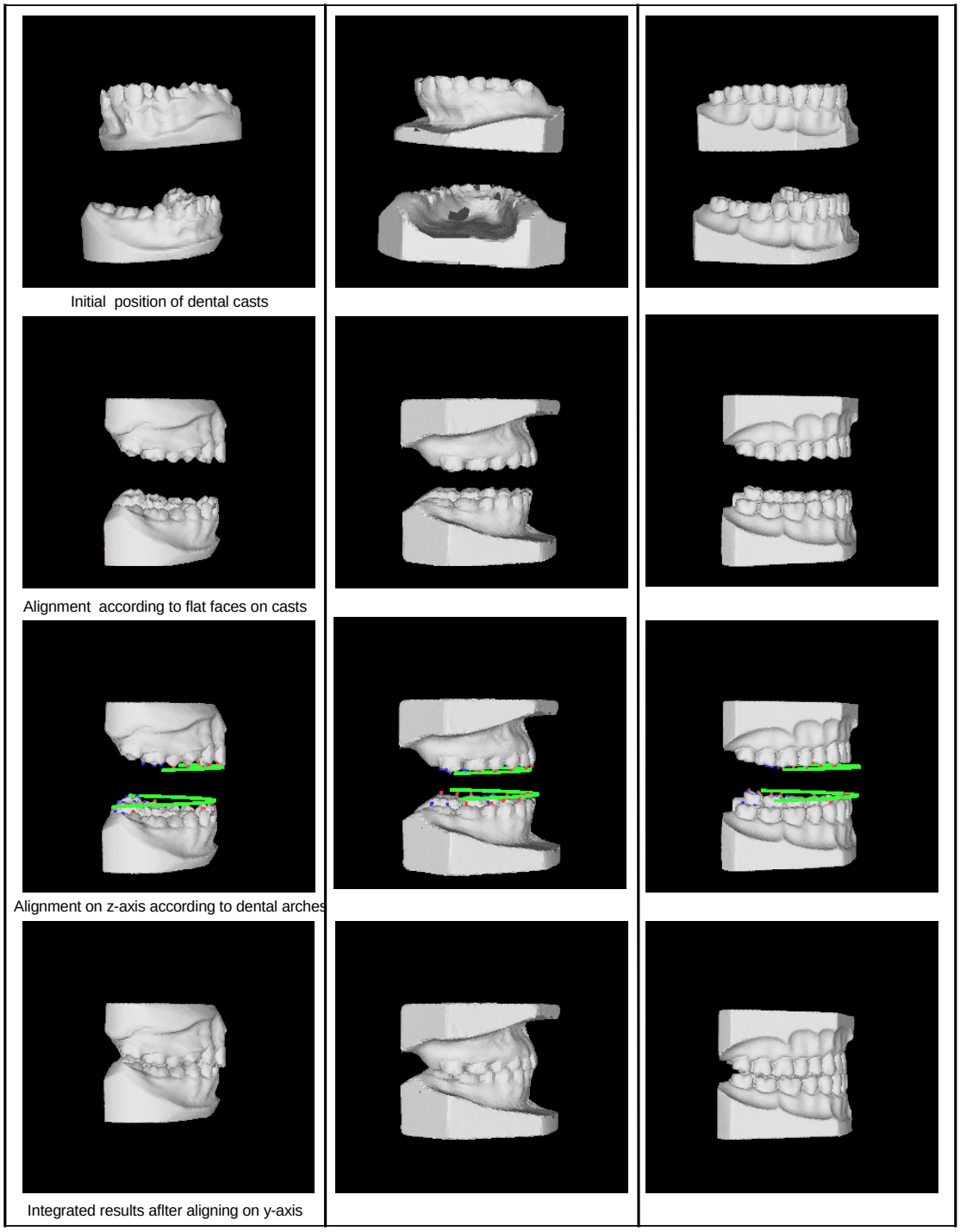

Figure 5.10: Columns (a), (b) and (c) represent the alignment procedure of three pairs of maxillary and mandibular casts.

5.4.2 Discussion

After the alignment of maxillary and mandibular dental casts, the integrated full dental casts should have such features: (1) its bottom is parallel with the *xz* plane; (2) its back surface is parallel with the *yz* plane. According to these, we can test the accuracy of the alignment. The result is shown in Table 5.4. We find the difference between the target angle and the actual angle is very small, less than 1°. Generally speaking, the desired accuracy for angle in medical images should be within an error range of $\pm 1^{\circ}$. Hence, the proposed method can be considered feasible and effective.

Table 5.4: The accuracy of the dental casts alignment.

Dental casts		Column (a)	Column (b)	Column (c)
Angle between the bottom and the *xz* plane	target value	0°	0°	0°
	actual value	0.090°	0.206°	0.539°
Angle between the back surface and the *yz* plane	target value	0°	0°	0°
	actual value	0.250°	0.234°	0.538°

5.5 Dentofacial Registration System

5.5.1 Experimental Goals

To test the validity of the developed dentofacial registration system, a new set of data is used as an input to the system. This new set of data likewise include: the lateral cephalogram, 3D dental and facial models.

The lower right angle between the functional occlusal plane and the porion-orbitale (Po-Or) plane, in a sense, indicates the spatial relationship of the dental and facial models (Figure 5.11). Here, both planes are perpendicular to the cephalogram. Additionally, the porion-orbitale plane passes through two landmarks on the cephalogram: porion (the highest point on the superior surface of the auditory meatus) and orbitale (a point located on the lowermost point on the outline of the bony orbit). The functional occlusal plane is where the upper and lower dental arches come into contact with each other. This plane bisects the intercuspation of the bicuspids and first molars and does not include the incisors. Hence, the accuracy of the registration system can be determined by comparing this common angle on the related cephalogram (θ) and on the 3D integrated dental and facial models (θ').

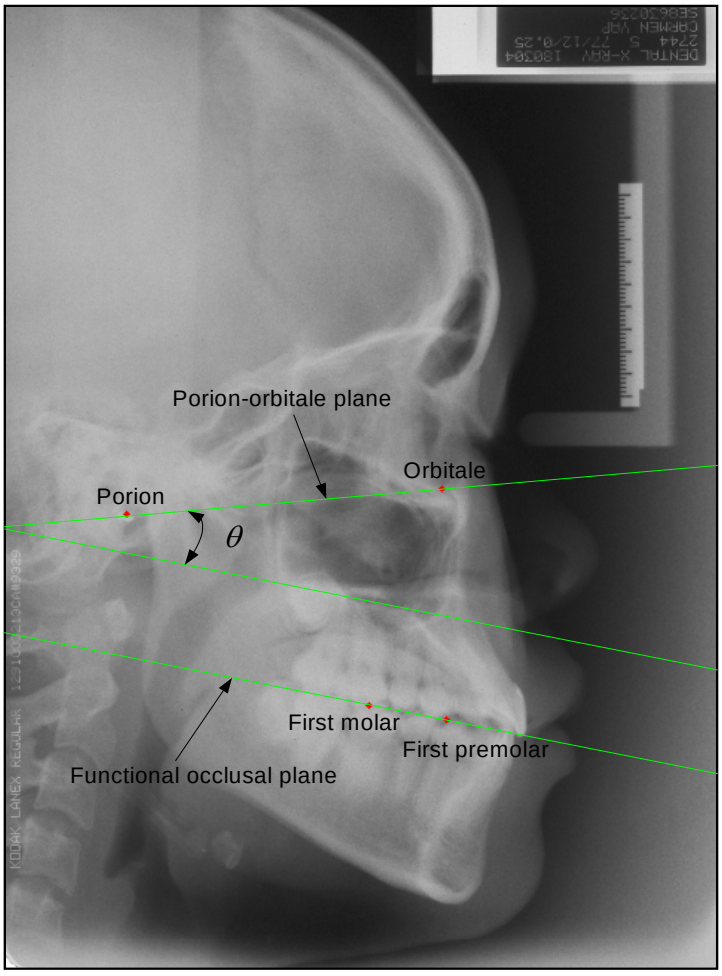

Figure 5.11: Reference points and planes used with lateral cephalograms.

5.5.2 Results and Discussion

The first step is to register the aligned maxillary and mandibular dental casts with the lateral cephalogram. The process and results are shown in Figure 5.12.

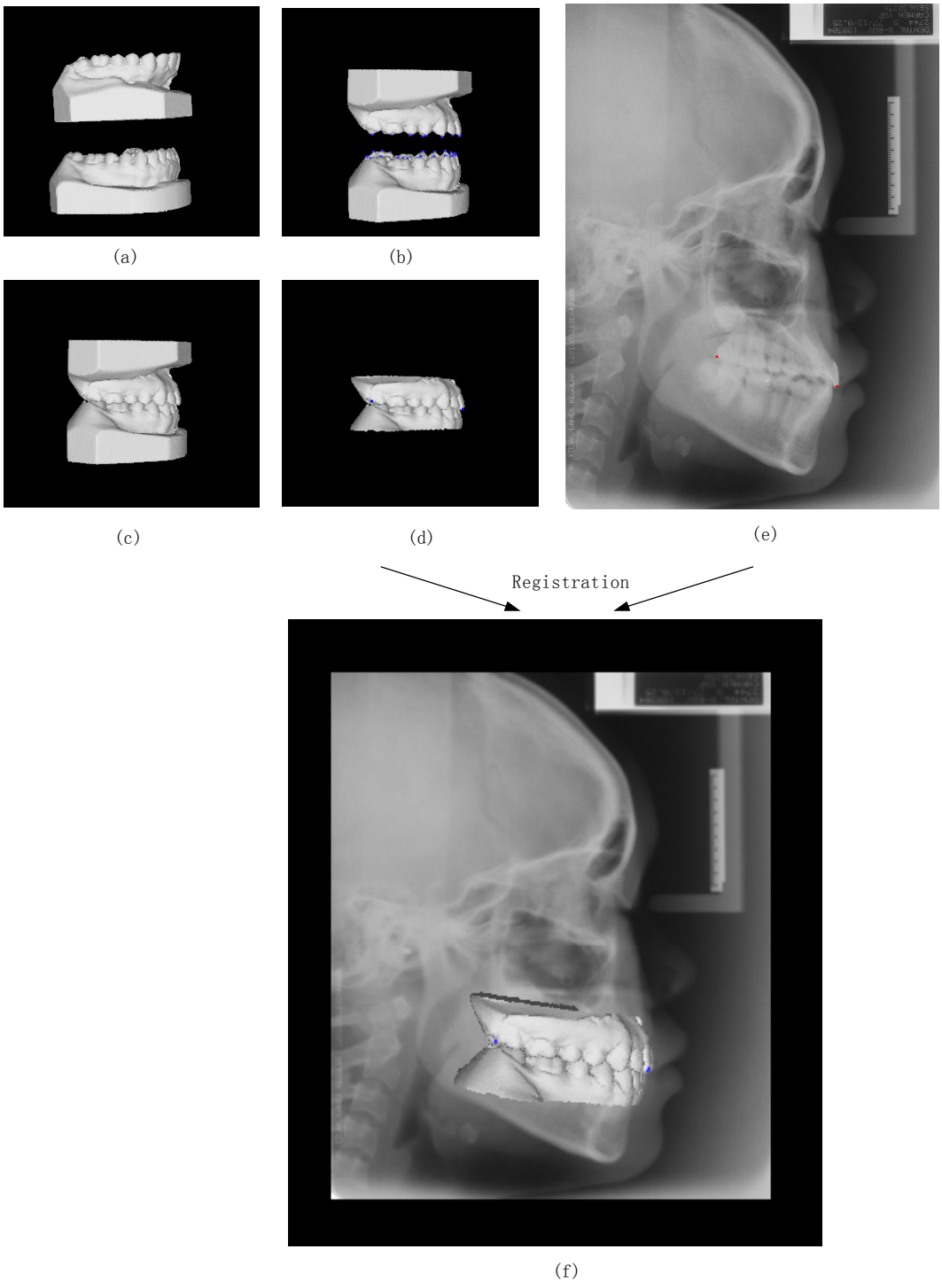

Figure 5.12: The registration result of dental casts and lateral cephalogram. Dental cast: (a) Initial position; (b) After rotation; (c) After translation; (d) Trimmed casts with landmarks. (e) X-ray with landmarks. (f) The registration result.

The second step is to register the facial shape model with the same cephalogram.

Figure 5.13 shows the registration result.

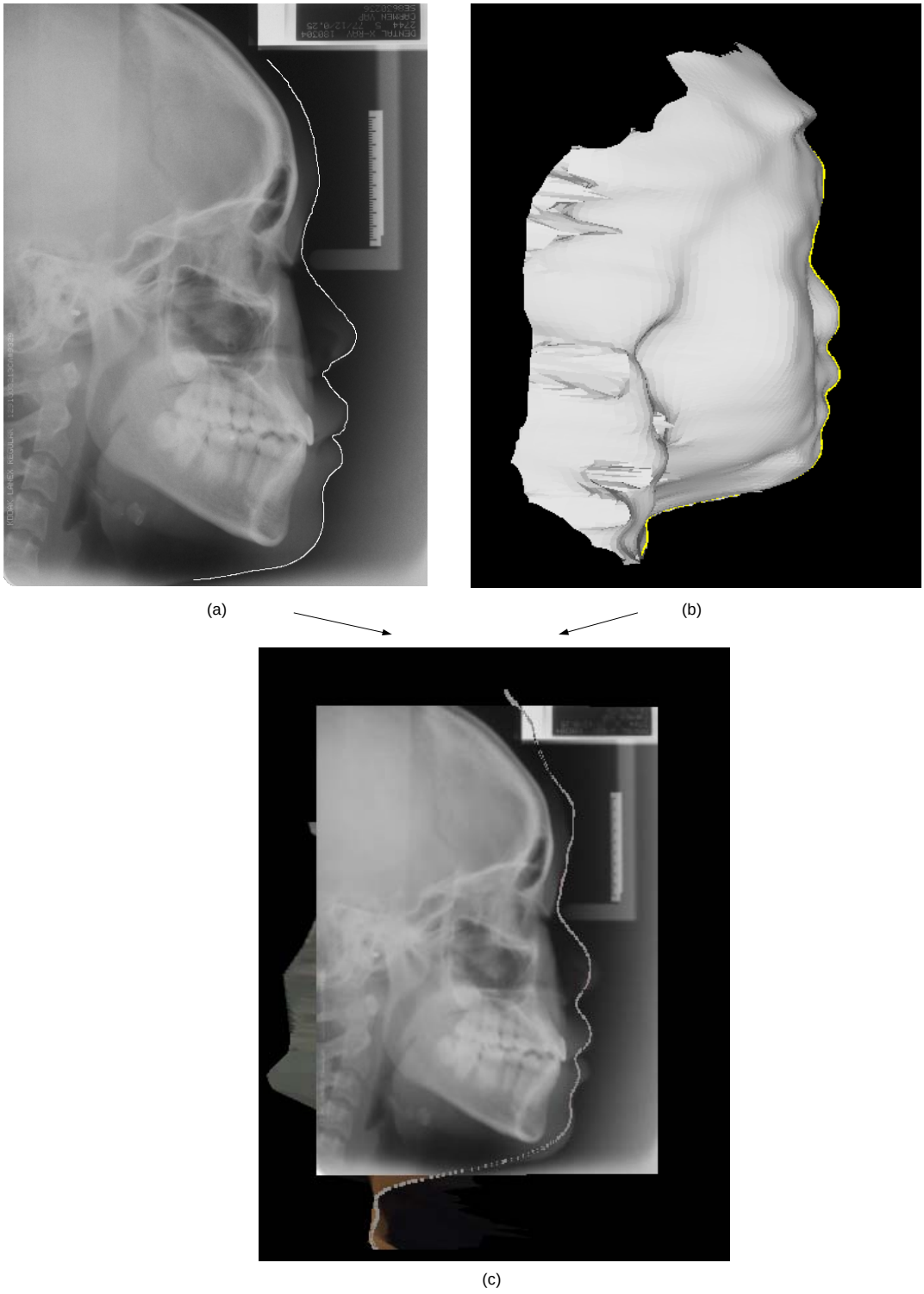

Figure 5.13: The registration result of facial model and lateral cephalogram. (a) Lateral cephalogram. (b) Facial model. (c) Registration result.

Finally, the 3D dental and facial data are integrated and visualized in Figure 5.14. And Table 5.5 gives the comparison of the angles θ and θ'.

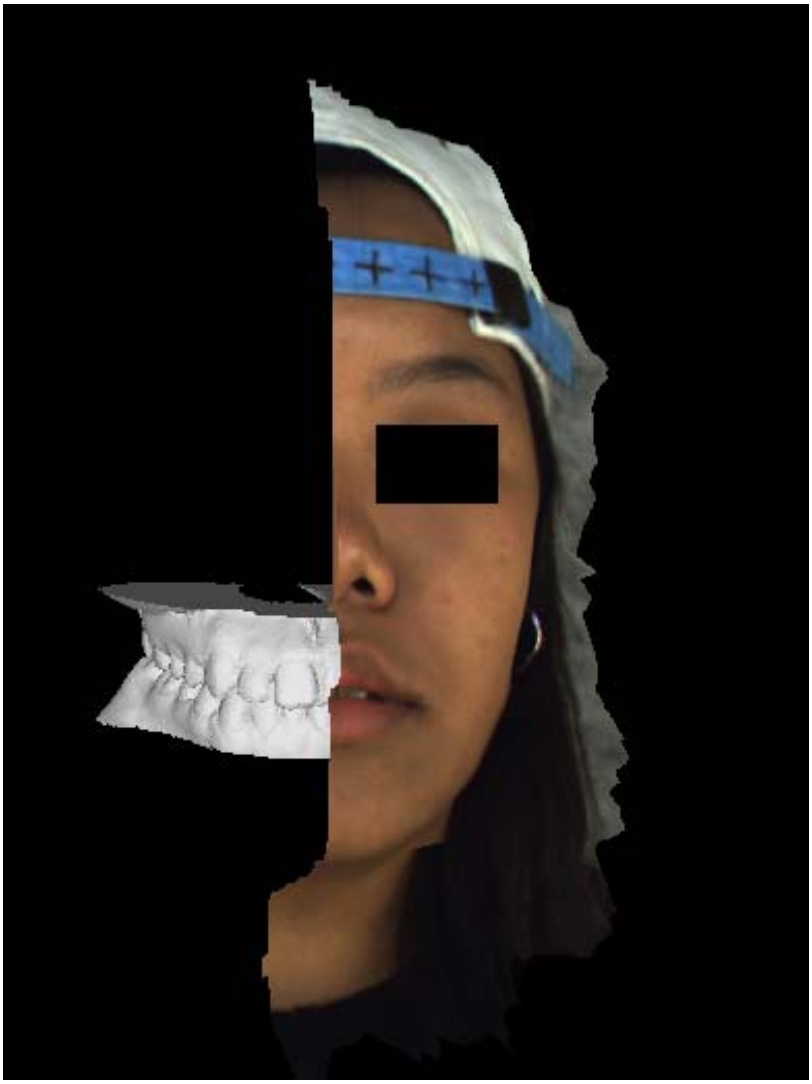

Figure 5.14: The integrated 3D dental and facial model

Table 5.5: Comparison of angles between the Po-Or plane and the occlusal plane

Occlusal plane angle to Po-Or plane		Value
On lateral cephalgoram	θ	15.7386°
On integrated dental and facial model	θ'	15.3847°
Angle difference	$\lvert\theta - \theta'\rvert$	0.3539°

In general, the desired angle tolerance is $\pm 1^{\circ}$ in such image registration. From Table 5.5, we can find there is a small difference ($0.3539^{\circ} < 1^{\circ}$) between the common angles on the related cephalogram (θ) and on the 3D integrated dental and facial models (θ'). That means after registration, the integrated dental and facial data shows the nearly correct spatial relationship of the dental cast and facial model.

However, the system's accuracy in the registration of 3D facial model with the lateral cephalogram is still hampered by the resolution of the 3D facial surface data. In order to observe the registration result in Figure 5.14 clearly, the important part is zoomed in Figure 5.15. As we can see, the nose and lips of the facial model are not as sharp as the real person. This is due to the *FaceVison* scanner we used is a kind of camera-based scanner, whose resolution may not be as high as a laser scanner. The deformation of these parts definitely influences the accurate registration of facial profiles extracted from the cephalogram and the facial model. To improve the accuracy of the registration, such deformation should be solved in the future work.

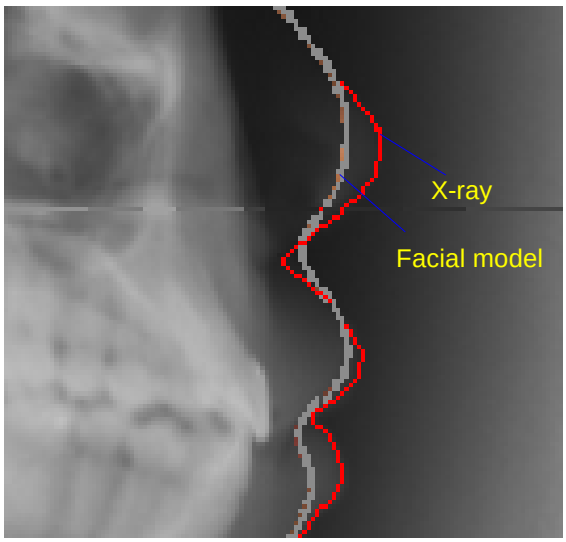

Figure 5.15: The deformation of the scanned facial model.

Chapter 6 Conclusion

This chapter concludes the thesis for our study and suggests how the project can be further improved.

6.1 Conclusion

A near-automatic dentofacial registration system has been implemented in this study. It realizes the registration and integration of the 3D facial shape model and dental casts with the help of 2D lateral cephalogram.

Both 3D models are registered separately with the lateral cephalogram to find the spatially geometric relationship. A facial-profile-based method is proposed to register the lateral cephalogram and the 3D facial model. A technique based on the detected landmarks is performed to register the dental cast and the lateral cephalogram. Finally, the 3D models are integrated and visualized simultaneously to assist the orthodontics in the diagnosis and treatment planning.

Four different types of experiments have been conducted to investigate the performance of the important intermediate steps involved in the dentofacial registration system. In the first experiment, the system's ability to extract facial profile from the lateral cephalogram and 3D facial model is tested and it is found that the system shows 87.5% accuracy in facial profile extraction. In the second experiment, the proposed facial-profile-based registration method, which determines the system's ability to superimpose a lateral cephalogram on the 3D facial model, is

examined by registering a facial profile and itself with different pose and size. We find the rotation error is much less than 1°, the scaling error is close to zero, and the translation error is within 1 to 2 pixels. The third experiment aims to test the alignment of maxillary and mandibular dental casts which is involved in the registration of dental casts with the cephalogram. In the last experiment, a new set of data is input to the registration system. The resultant integrated image is studied and the system accuracy is measured by the angle between the Po-Or plane and the occlusal plane. The error of this angle is 0.3539°, which is quite small and within the standard tolerance (1°).

6.2 Future work

Our results show that the proposed dentofacial registration system has the potential to provide the orthodontists with a virtual 3D dental and facial environment for orthodontic diagnosis and treatment planning. However, the system's accuracy in the registration of 3D facial model with the lateral cephalogram is hampered by the resolution of the 3D facial surface data. The nose and lips displayed in the scanned facial data are not as sharp or accurate as they are in the real life. This is due to the *FaceVison* scanner we used is a camera-based, whose resolution may not be as high as a laser scanner. In order to improve our system's performance, the deformation function applied to the 3D facial model can be considered to be developed in future work (Appendix C).

The registration of the dental casts and lateral cephalogram is implemented by a semi-automatic method. The maxillary and mandibular dental casts are aligned and integrated automatically, but the landmarks on the dental casts and cephalogram are selected manually for the registration. Hence, it is suggested that an automatic method be developed for the landmarks extraction in future work.

Furthermore, subsequent enhancements to this registration system may take the form of merging accurate 3D root shapes to the 3D crowns of the teeth on the dental casts. Simulation of tooth movements within the created 3D virtual dental and facial environment will permit the clinician to visualize how the changes in the spatial position of the teeth affect the spatial position of the lips and facial contours.

References

[1] http://www.isds.org/publicInfo/Careers/DentalSpecialties.asp.

[2] R. Enciso, A. Memon, U. Neumann, and J. Mah, The virtual cranio-facial patient project, *Proc. 3D MODELLING 2003, MEDICAL3D session, Harbour Conference*, pp. 1-10, 2003.

[3] S. Baumrind, S. Curry, S. Carlson, A. Beers, and R.L. Boyd, Using three-dimensional imaging to assess treatment outcomes in orthodontics: a progress report from the University of the Pacific, *Orthodontics and Craniofacial Research* 6 (Suppl. 1), pp. 132-142, 2003.

[4] D.M. Sarver, *Esthetic orthodontics and orthognathic surgery* (Mosby, 1998).

[5] M.Y. Hajeer *et al.*, Three-dimensional imaging in orthognathic surgery: The clinical application of a new method, *International Journal of Adult Orthodontics & Orthognathic Surgery*, vol. 17, no. 4, pp. 1-13, 2002.

[6] N. Noguchi and M. Goto, Computer simulation system for orthognatic surgery, *Orthodontics and Craniofacial Research* 6 (suppl. 1), pp. 176-178, 2003.

[7] Lisa Gottesfeld-Brown, A survey of image registration techniques, *ACM Computing Surveys*, vol. 24, no. 4, pp. 325-376, 1992.

[8] C.R. Maurer and J.M. Fitzpatrick, A review of medical image registration, in Interactive Image-Guided Neurosurgery, *American Association of Neurological Surgeons*, vol. 4, pp. 17-44, 1993.

[9] J.B.A. Maintz and M.A. Viergever, A survey of medical image registration, *Medical Image Analysis*, vol. 2, no. 1, pp. 1-36, 1998.

[10] P.A. Van der Elsen, E.J.D. Pol, and M.A. Viergever, Medical image matching – a review with classification, *IEEE Engineering in Medicine and Biology*, vol. 3, pp. 26-39, 1993.

[11] J.M. Fitzpatrick, D.L.G. Hill, and C.R. Maurer, Handbook of Medical Imaging, vol. 2, SPIE Press, 2000.

[12] D.L.G. Hill *et al.*, Accurate frameless registration of MR and CT images of the head: Applications in surgery and radiotherapy planning, *Radiology*, vol. 191, pp. 447-454, 1994.

[13] M.Y. Wang, J.M. Fitzpatrick, and C.R. Maurer, Design of fiducials for accurate registration of CT and MR volume images, *Medical Imaging 1995: Image Processing, Proc. SPIE* vol. 2434, pp. 96-108, 1995.

[14] P.J. Besl and N.D. Mc Kay, A method for registration of 3D shapes, *IEEE Transactions on Pattern Analysis and Machine Intelligence*, vol. 14, no. 2, pp. 239-256, 1992.

[15] D.L.G. Hill and D.J. Hawkes, Voxel similarity measures for automated image registration, *Visualization in Biomedical Computing 1994*, *Proc. SPIE* vol. 2359, pp. 205-216, 1994.

[16] F. Maes, A. Collignon, D. Vandermeulen, G. Marchal, and P. Suetens, Multimodality image registration by maximization of mutual information, *IEEE Transactions on Medical Imaging*, vol. 16, no. 2, pp. 187-198, 1997.

[17] W.M. Wells, III, P. Viola, H. Atsumi, S. Nakajima, and R. Kikinis, Multi-modal volume registration by maximization of mutual information, *Medical Image Analysis*, vol. 1, pp. 35-51, 1996.

[18] J. Feldmar, N. Ayache, and F. Betting, 3D-2D projective registration of free-form curves and surfaces, *Computer Vision and Image Understanding*, vol. 65, pp. 413-424, 1997.

[19] C.M. Cyr, A.F. Kamal, T.B. Sebastian, and B.B. Kimia, 2D-3D registration based on shape matching, *Mathematical Methods in Biomedical Image Analysis, IEEE Proceedings*, pp. 198-203, 2000.

[20] L.D. Harmon, M.K. Khan, R. Lasch, and P.F. Ramig, Machine identification of human faces, *Pattern Recognition*, vol. 13, no. 2, pp. 97-110, 1981.

[21] L.D. Harmon, S.C. Kuo, P.F. Ramig, and U. Raudkivi, Identification of human face profiles by computer, *Pattern Recognition*, vol. 10, pp. 301-312, 1978.

[22] N. Okamoto, W. Chen, N. Iida, and T. Minami, Automatic extraction of contour lines and feature points from profile images. *Proceedings of the IEEE Canadian Conference on Electrical and Computer Engineering - Engineering Innovation: Voyage of discovery*, vol. 2, pp. 831-834, 1997.

[23] B. Dariush, S.B. Kang, and K. Waters, Spatiotemporal analysis of face profiles: Detection, segmentation, and registration, *In Proceedings of the 3rd IEEE International Conference on Automatic Face and Gesture Recognition*, pp. 248-253, 1998.

[24] J.C. Campos, A.D. Linney, and J.P. Moss, The analysis of facial profiles using scale space techniques. *Pattern Recognition*, vol. 26, no. 6, pp. 819-824, 1993.

[25] E.A. Johnson and C. Wu, A real-time fuzzy logic-based neural facial feature extraction technique, *Proceedings of the Third IEEE Conference on Fuzzy Systems*, vol. 1, pp. 268-273, 1994.

[26] T. Akimoto, Y. Suenaga, and R.S. Wallace, Automatic creation of 3D facial models, *IEEE Computer Graphics and Applications*, vol. 13, no. 5, pp. 16-22, 1993.

[27] N.V. Agfa-Gevaert, *Arcus II Scanner Owners Guide*, 1994.

[28] D. Lec, Edge detection, classification and measurement, *Proc. IEEE Computer Society Conference on Computer Vision and Pattern Recognition*, pp. 2-10, 1989.

[29] J. Canny, A computational approach to edge detection, *IEEE Transactions on Pattern Analysis and Machine Intelligence*, vol. 8, no. 6, pp. 679-698, 1986.

[30] L.A. Spacek, Edge detection and motion detection. *Image and Vision Computing*, vol. 4, no. 1, pp. 43-56, 1986.

[31] M. Petrou and J. Kittler, Optimal edge detectors for ramp edges, *IEEE Transactions on Pattern Analysis and Machine Intelligence*, vol. 13, no. 5, pp. 483-491, 1991.

[32] N. Otsu, A threshold selection method from gray-level histograms, *IEEE Transactions on Systems, Man, and Cybernetics*, vol. 9, no. 1, pp. 62-66, 1979.

[33] W.H. Press *et al.*, Numerical Recipes in C: The Art of Scientific Computing, Cambridge University Press, 1988-1992.

[34] D.M. Wuescher and K. L. Boyer, Robust Contour Decomposition Using a Constant Curvature Criterion, *IEEE Transactions on Pattern Analysis and Machine Intelligence*, vol. 13, no. 1, pp. 41-51, 1991.

[35] S. Umeyama, Least-squares estimation of transformation parameters between two point patterns, *IEEE Transactions on Pattern Analysis and Machine Intelligence*, vol. 13, no. 4, pp. 376-380, 1991.

[36] W.Y. Mok, Pose estimation of teeth through crown-shape matching, Mater's thesis, National University of Singapore: Electrical and Computer Engineering Department, 2002.

[37] http://www.cyber-site.co.uk/3030specs.htm.

[38] http://www.inition.co.uk/inition/product_digiscan_geomatrix_facevision.htm.

[39] S. Yoshizawa *et al.*, A simple approach to interactive free-form shape deformations, *Proceedings of the 10th Pacific Conference on Computer Graphics and Applications*, pp. 471-474, 2002.

Appendix A

Singular Value Decomposition

SVD methods [33] are based on the following theorem of linear algebra: Any $M \times N$ matrix $\mathbf{A}$ whose number of rows M is greater than or equal to its number of columns N, can be written as the product of an $M \times N$ column-orthogonal matrix $\mathbf{U}$, an $N \times N$ diagonal matrix W with positive or zero elements (the singular values), and the transpose of an $N \times N$ orthogonal matrix $\mathbf{V}$. The various shapes of these matrices will be made clearer by the following equation:

$$\begin{pmatrix} & \\ & \mathbf{A} \\ & \end{pmatrix} = \begin{pmatrix} & \\ & \mathbf{U} \\ & \end{pmatrix} \cdot \begin{pmatrix} w_1 & & & \\ & w_2 & & \\ & & \ddots & \\ & & & w_N \end{pmatrix} \cdot \begin{pmatrix} & \\ & \mathbf{V}^T \\ & \end{pmatrix} \qquad (1)$$

The matrices $\mathbf{U}$ and $\mathbf{V}$ are each orthogonal in the sense that their columns are orthonormal,

$$\sum_{i=1}^{M} U_{ik} U_{in} = \delta_{kn} \qquad \begin{matrix} 1 \le k \le N \\ 1 \le n \le N \end{matrix} \qquad (2)$$

$$\sum_{i=1}^{M} V_{ik} V_{in} = \delta_{kn} \qquad \begin{matrix} 1 \le k \le N \\ 1 \le n \le N \end{matrix} \qquad (3)$$

or

$$\begin{pmatrix} \\ \mathbf{U}^T \\ \\ \end{pmatrix} \cdot \begin{pmatrix} \\ \mathbf{U} \\ \\ \end{pmatrix} = \begin{pmatrix} \\ \mathbf{V}^T \\ \\ \end{pmatrix} \cdot \begin{pmatrix} \\ \mathbf{V} \\ \\ \end{pmatrix} = \begin{pmatrix} \\ 1 \\ \\ \end{pmatrix} \quad (4)$$

Since $\mathbf{V}$ is square, it is also row-orthonormal, $\mathbf{V} \cdot \mathbf{V}^T = 1$.

The SVD decomposition can also be carried out when $M < N$. In this case the singular values w_j for $j = M+1, \cdots, N$ are all zero, and the corresponding columns of $\mathbf{U}$ are also zero. Equation (2) then holds only for $k, n \le M$.

The decomposition (1) can always be done, no matter how singular the matrix is, and it is "almost" unique. That is to say, it is unique up to (a) making the same permutation of the columns of $\mathbf{U}$, elements of $\mathbf{W}$, and columns of $\mathbf{V}$ (or rows of $\mathbf{V}^T$), or (b) forming linear combinations of any columns of $\mathbf{U}$ and $\mathbf{V}$ whose corresponding elements of $\mathbf{W}$ happen to be exactly equal. An important consequence of the permutation freedom is that for the case $M < N$, a numerical algorithm for the decomposition need not return zero w_j's for $j = M+1, \cdots, N$; the $N - M$ zero singular values can be scattered among all position $j = 1, 2, \cdots, N$.

Appendix B

FaceVision 600 Scanner

The FaceVison 600 series scanner produced by Geometrix company provides an automated solution for full 180-degree ear-to-ear 3D facial imaging. The scanner consists of six high-speed IEEE-1394 “Firewire” cameras mounted in a rigid frame containing a complete optimized lighting system. The cameras are arranged in three pairs, each of which captures a 3D image from one view of the subject's face (front, right, and left). Acquisition is complete in less than a second, and then the three patches are merged together into a single surface, holes are filled, the surface is smoothed, and a seamless texture is applied by blending image data from all the views. The result is a finished ear-to-ear 3D facial model. The 600 Series' automated 3D processing software eliminates extensive manual clean-up needed in other 3D facial imaging system.

The scanning system selects the Viewpoint Metastream format as the default export, so after scanning and computation, the program automatically pops up a browser window with a preview of the 3D model. Also, the user can export the data as other formats. The following formats are supported:

- Viewpoint Metastream
- 3D Studio
- Alias Wavefront
- Autodesk DXF
- W3C VRML

In our project, the 3D face surface data is exported in VRML format with a filename extension of *.wrl*, short for "world". VRML is an ASCII format for describing 3D objects and interactive environment. The advantages of using VRML files are as follows:

- VRML is an ISO standard.
- Texture information can be embedded.
- Most systems can export the object geometry in VRML.
- VRML format is an platform neural ISO/IEC standard designed for the Internet.
- Can be displayed by most of the existing browsers.

Appendix C

3D Surface Deformation

Because the *FaceVison* scanner we used is a camera-based, whose resolution may not be as high as a laser scanner, the nose and lips of the scanned facial data are not as sharp and accurate as they are in the real life. This inevitably hampers the performance of the developed dentofacial registration system. The deformation function is sought to improve the 3D facial model.

Yoshizawa et al. [39] proposed a set of free-form shape deformation techniques. Given a suface represented by a mesh and a control point, for every mesh vertex the difference between the control point and the vertex is considered. The vertex is shifted by a displacement equal to the difference times a scale factor where the scale factor is given by a function depending nonlinearly on the difference. The function is bump-shaped and depends on a number of parameters. Varying the parameters leads to a rich palette of shape deformations. The proposed approach includes also shape deformations with multiple (real, auxiliary, and virtual) control points and constrained, directional, and anisotropic deformations. It allows a user to edit a given shape interactively and intuitively. No mesh connectivity information is used and, therefore, the proposed techniques can be applied directly to a shape given as a cloud of points.

We tried the software developed by them to sharpen the nose part in our scanned facial shape model. Figure 1A shows the original image, and Figure 2A shows the result image after deformation. It was found the nose was sharpened to be more

natural, and can be mapped with the cephalogram exactly. For the lips, although they did not reach their actual shape, they are actually improved significantly. This experiment indicated that the deformation of the facial shape model is feasible, and it would improve the performance of our dentofaical registration system.

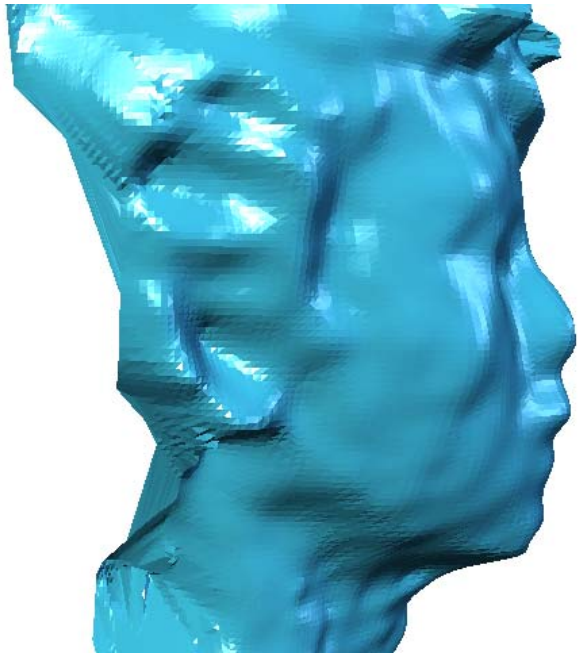

Figure 1A: The original facial model.

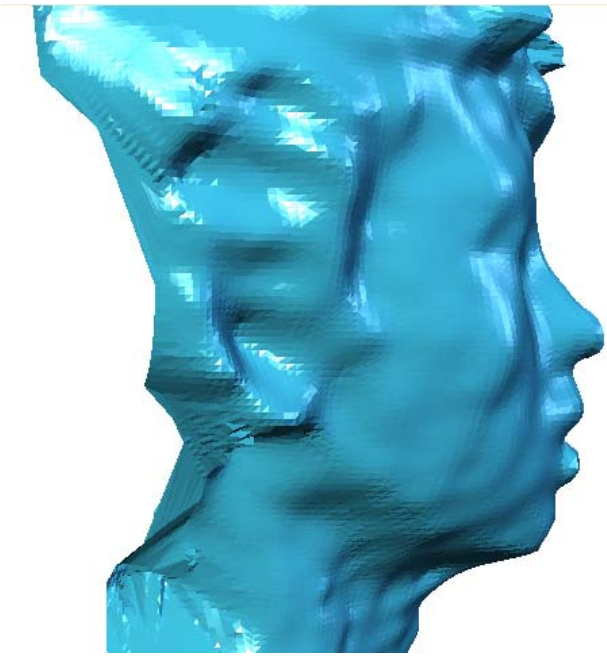

Figure 2A: The facial model with the deformed nose.

After the deformation of 3D facial model, the 2D facial profile is extracted according to the method presented in Chapter 3. Figure 3A shows the result. As we can see, the nose and lips are sharpened and closer to the actual facial profile. By registering the deformed model with the cephalogram, we obtain a better result (Figure 4A) compared to Figure 3.29.

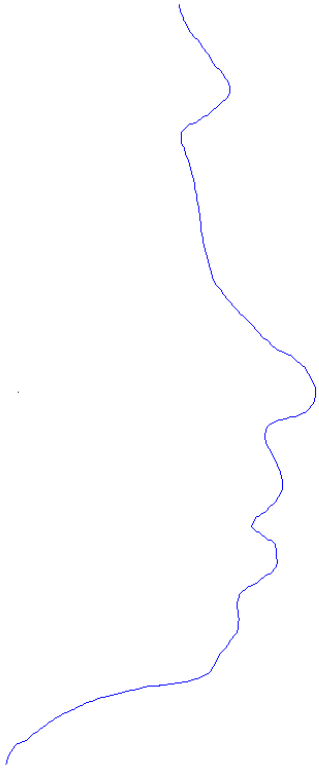

Figure 3A: The facial profile extracted from the deformed model.

Figure 4A: The registration result of the deformed model with lateral cephalogram.